COO-3476-11

State University of New York
at Stony Brook
Stony Brook, New York 11790

College of Engineering
Department of Materials Science
telephone: (516) 246-6759

StonyBrook

INTERSTITIAL IMPURITY INTERACTIONS AND DISLOCATION MICRODYNAMICS IN Mo CRYSTALS

by

Dora Ng Kwok

U.S. Energy Research and Development Administration

Contract No. AT-(11-1)-3476

Report No. COO-3476-11

MASTER

INTERSTITIAL IMPURITY INTERACTIONS AND DISLOCATION MICRODYNAMICS IN Mo CRYSTALS

A thesis presented

by

Dora Ng Kwok

to

The Graduate School
in partial fulfillment of the requirements
for the degree of
Master of Science

in

Engineering
Department of Materials Science
State University of New York
at
Stony Brook
May 1975

DISTRIBUTION OF THIS DOCUMENT UNLIMITED

STATE UNIVERSITY OF NEW YORK

AT STONY BROOK

THE GRADUATE SCHOOL

Dora Ng Kwok

We, the thesis committee for the above candidate for the M.S. degree, hereby recommend acceptance of the thesis.

John C. Bilello
(Chairman & Advisor) John C. Bilello

Franklin F.Y. Wang Franklin F.Y. Wang

Patrick J. Herley Patrick J. Herley

Herbert Herman
(Chairman, Department of
Materials Science)

The thesis is accepted by the Graduate School.

Abstract of the Thesis

INTERSTITIAL IMPURITY INTERACTIONS AND DISLOCATION MICRODYNAMICS IN Mo CRYSTALS

by

Dora Ng Kwok

Master of Science

in

The College of Engineering

Department of Materials Science

State University of New York at Stony Brook

The effect of interstitial impurities on the mechanical properties of molybdenum are explored in this investigation by comparing results obtained for crystals of various interstitial contents controlled by ultra-high vacuum outgassing. Results show a 6% modulus reduction for as-grown samples and a 13% decrease for outgassed specimens at low applied stresses. As a function of plastic microstrain, the values of modulus defect for both as-grown and outgassed specimens saturate at the same value.

Interstitial impurities act as pinning agents to dislocation bowing, but when all the easy dislocation loops have brokenaway from local interstitial pins, the modulus defect reaches a constant saturation value.

Etch pitting techniques were used to correlate microstrain observations with dislocation generation and motion. It has been found that edge dislocation generation and movement are active in the microstrain region while screw dislocations are relatively inactive until the macrostrain region is reached. Dislocation velocities range from 10^{-6} to 10^{-3} cm/sec and the average distance between interstitial impurity pinning points is found to be $\sim 8 \times 10^{-4}$ cm.

TABLE OF CONTENTS

LIST OF FIGURES

<u>Figure</u> <u>Page</u>

LIST OF TABLES

LIST OF SYMBOLS

σ – stress amplitude

σ_A – anelastic stress limit

σ_E – elastic limit

ε_p – plastic strain

$\dot{\varepsilon}_p$ – plastic strain rate

τ^* – resolved shear stress

E_D – dynamic modulus

E_R – relaxed modulus

S_{ij} – compliance

l – loop length between pinning points

b – Burger's vector

N – number of dislocations

$\dot{N}$ – number of dislocations generated

v – dislocation velocity

a – lattice parameter

U_o – binding energy for dislocation breakaway

c_N – concentration of N in atomic %

c_O – concentration of O in atomic %

p_{N_2} – N_2^+ partial pressure

P_{O_2} – O_2^+ partial pressure

ΔG_T – free energy of formation

E – edge

S – screw

T – temperature in °K

ppm – part per million

UHV – ultra-high vacuum

EDM – electron discharge machine

EBZR – electron beam zone refined

PPG – partial pressure gas-analyzer

D – ultra-high vacuum degassed

A – as-grown

ACKNOWLEDGMENTS

My sincere gratitude goes to Prof. J.C. Bilello who spent many long hours guiding and advising me during this investigation. I would like to thank Mr. R. Cole and Mr. V. Rontino for their technical assistance and Dr. John M. Liu for growing the crystals. Lastly, I wish to thank my husband, Patrick, for his assistance and encouragement in making this work possible.

I would also like to acknowledge the U.S. Energy Research and Development Administration for their support, under Contract No. AT (11-1) - 3476.

§1. INTRODUCTION

Molybdenum is a refractory metal with vast technological importance. However, its applications are limited by its insufficient fracture toughness. The fracture toughness is intimately related to its ability to generate and sustain plastic deformation during crack initiation and propagation. Therefore, it is of critical interest to understand the factors which inhibit plastic relaxations in such a BCC metal. Many theories have been proposed during the past decade, the principle theories fall into four categories: the effect of interstitial impurities (1-3), the inherent BCC lattice (4), the effects of slip asymmetry (5,6), and anisotropy in flow between edge and screw dislocations because of core splitting of screw dislocations (7).

1.1 Review of Previous Experimental Results

The mechanical properties of molybdenum, like other BCC metals, are strongly influenced by impurities, especially at low temperatures. To understand the inherent behavior of these metals, it is essential to eliminate, as much as possible, their substitutional and interstitial impurities. Work on molybdenum is limited, but other BCC metals, like tungsten, which is believed to behave in a similar fashion to molybdenum, have been studied.

The effect of substitutional impurities on the tensile properties of tungsten single crystals at temperatures between 77°K and 302°K has been reported by Koo (8). The critical resolved shear stress was decreased, at all temperatures, by increasing the number of zone-melting passes from one to five. Ductility was reported to increase with the number of zone passes, while twinning was facilitated. Yield stresses of molybdenum single crystals have also been shown to decrease with increasing number of zone passes (3).

Interstitial impurities contribute significantly to the mechanical properties of BCC metals. In molybdenum single crystals, the critical resolved shear stress and its temperature dependence decreased with increasing interstitial purity, although ductility was not improved by purification using ZrH_2 as a gettering agent (1), instead of vacuum outgassing, which will be employed in the present investigation. However, ductility was determined by reduction in area calculations, and in some cases, the reduction in area was found to be as high as 100% (78^{o}K) and as low as 9% (20^{o}K). The yield point return and modulus defect recovery of unalloyed, recrystallized, powder metallurgy molybdenum (9), were attributed to a pinning process with similar kinetics as the Cottrell-Bilby model, where interstitials diffuse towards dislocations and are bound to the dislocation lines. (In this process, dislocation generation can only be possible when sufficient energy is applied to unbind such pinning).

Interstitial levels in the parts per million (ppm) range have profound effects on mechanical behavior as well as the inherent lattice itself having interaction energies with dislocations of the same order of magnitude as with impurities. It is therefore imperative that sensitive techniques be used to distinguish between the different mechanisms. The present work will employ techniques using etch pit observations, capable of revealing dislocation flow more or less on a one-to-one basis, as well as ultra-high sensitivity microstrain methods (4, 10-13) to magnify the stress-strain behavior in a way that can be readily correlated to etch pit observation. It is believed that such a sensitive technique should be able to examine the initial stages of dislocation generation and mobility and elaborate on factors which impede such activation. Thermal assistance can be minimized by using low temperature testing methods. Different temperature dependences are expected for different mechanisms, thus, low temperature mechanical results will aid in identifying the type of damping mechanism that is predominant in BCC molybdenum.

It has been found, in molybdenum, that there exists an asymmetry for slip on $\{112\}$ planes (5). The critical resolved shear stress for slip on the hard $\{112\}$ planes is reported to be at least twice the critical resolved shear stress for slip on $\{110\}$ planes. According to Guiu (5), slip on $\{110\}$ planes is always observed. Thus, independent of orientation, the yielding process involves slip on the {110}<111> system. During cyclic deformation of molybdenum single crystals (6), the saturation stress in tension is different from that in compression, which suggests the presence of an asymmetry of the flow stress. Asymmetry of slip is believed to be present as soon as plastic strain becomes detectable. <110>crystals are reported to be harder in tension than in compression while the reverse is reported for <100> crystals (6). The above-mentioned observations will be compared to the results obtained from this investigation and the slip systems that affect microyielding will be discussed.

According to Vitek et al (7), slip geometry, particularly the asymmetry of slip, is controlled by the screw dislocation core structure, and is similar for many BCC metals. The core structure is described by splitting on three {112} planes in the twinning directions, with large displacements on three {110} planes that decrease monotonically. When screw dislocations are moved by an applied stress, the core structure may have to be changed into a glissile configuration, or they can move by direct jumps between stable configurations. The dislocation center always coincides with a three-fold screw symmetry axis, so that $\{110\}$ and $\{112\}$ are the only microscopic slip planes (7). It is suggested that displacement will be concentrated on the three $\{110\}$ planes radiating from the center and these will be the predominant slip planes in BCC metals. Etch pit results obtained in the present experiment will be analysed in light of the above findings and the mechanisms governing microslip will be explored.

1.2. Experimental Plan

Interstitial impurities in the ppm range can have a profound effect upon the mechanical properties of BCC metals, as examples above have shown. Therefore, it is necessary to minimize the interstitial content as much as possible in order to have some base level for studying the inherent properties of the BCC lattice. Single crystals of molybdenum will be tested in compression at 77°K and 298°K. Edge and screw dislocation generation and motion will be observed using relatively one-to-one etch pitting techniques. Etch pit results will then be correlated to the microstrain behavior. The interstitial concentration of these single crystals will be minimized by ultra-high vacuum degassing. Similar etch pit and microstrain studies will be performed and the results for as-grown and outgassed specimens will be compared.

Compression testing methods are preferred to tension experiments due to a number of advantages of the former technique. Material is conserved and a much larger amount of data can be generated and compared. There is no gripping problem and a uniform stress system can be produced. However, drawbacks do exist in relating the distance moved by the compression plates and the true strain produced in the specimen. This will be discussed in section 2.6.

Comparison of results of as-grown and outgassed crystals should display the influence of interstitial impurities on the mechanical behavior of BCC molybdenum. The behavior of the metal is, to a great extent, dependent on the number and type, edge or screw, of dislocations present, but a large number of reports do not give any information on the dislocation densities and distributions of test samples. In this investigation, the distribution of dislocations, edge and screw, will be examined before and after load-unload cycling, with special observation on the generation and motion of both types of dislocations. The contribution of each type of dislocation to slip initiation will be explored in conjuction with studies of the effect of interstitial impurities as they affect edge-screw multiplication and mobility.

§2. EXPERIMENTAL PROCEDURE

The experimental techniques employed in this investigation are described in the following six sections. Single crystals of BCC molybdenum were prepared to possess the desired purity levels and were tested in compression. Dislocation generation and motion were explored using etch pitting techniques.

2.1. Crystal Preparation

Three-pass single crystals of molybdenum, ~3.2 mm in diameter, were grown in an MRC electron beam zone refining (EBZR) unit at a pressure of ~10^{-6} torr. One-pass single crystals were grown similarly and were used as preliminary test samples. Three types of orientation of the compression axis were employed, namely, <110>, <111> , and <100> , for type A, B, and C crystals, respectively. All these orientations are less than 2° away from the corners of a standard projection, as verified by Laue back-reflection photographs. The compression axis, glide plane and surface, edge and screw surfaces of the

<110> type crystals are shown in Fig. 1.

Due to the zone-refining process, the diameters of some crystals were off-centered by ~0.025 mm. In order to obtain uniform stress distribution over the entire cross-section of the specimen, a diameter-turning process was performed. This was accomplished by mounting the crystal to a semi-hollow ball bearing with Aremco Crystal Bond and rotating them at ~60 rpm. A flat copper electrode was used on an ELOX electron discharge machine (EDM) to remove those parts of the crystal that were off-centered. Electrical contact to sample was insured using silver paint. Specimens to be outgassed in vacuum were hole-drilled on the EDM using a tungsten wire electrode ~0.8 mm in diameter. This was performed so as to allow the specimens to be hung, with a tungsten wire, inside an electron beam furnace mounted in an ultra-high vacuum chamber for outgassing. Description of the electron beam furnace appears elsewhere (14).

2.2 Purification Procedure

In order to understand the intrinsic

behaviour, and to also obtain information on the nature of interstitial impurities, it was desirable, to eliminate, as much as possible, the interstitial impurities of some specimens and compare their mechanical properties to the as-grown samples. This was performed by outgassingin ultra-high vacuum.

To avoid recrystallization, specimens that had been treated in the EDM were polished, to remove any damage due to spark erosion, before they were outgassed for 60 hours at 2673°K. The electron beam furnace was capable of allowing up to 154 mm of crystal in a total base pressure of 10^{-10} torr. The steady state total pressure, at the end of degassing, was $\sim 5\times10^{-9}$ torr, as measured with a digital ionization gage. A mass-spectrometer-partial pressure gas analyzer (PPG) was connected to the system and was used to monitor the partial pressures of elements from 1 to 70 amu. Mass scans were made at regular intervals during degassing to ensure its effect. Particular attention was paid in observing the oxygen, O_2^+, and nitrogen, N_2^+, peaks.

2.3. Specimen Sectioning

The as-grown and outgassed crystals were cut into sections ~7.5 mm in length on the EDM. The cut specimens were then slip-fitted into a tungsten carbide disk for mechanical polishing. The disk was ground flat and parallel, with a diamond wheel, to within ±0.0025 mm over its 25.4 mm diameter and was drilled with a series of holes, using different sizes of tungsten electrodes, ranging from 2.7 to 3.3 mm in diameter. The ends of the specimens were held in the disk by some Aremco Crystal Bond, and polished mechanically by using silicon carbide paper and alumina successively. Photographs of the polishing rig are shown in Fig. 2. Approximately 0.25 mm of crystal were taken off each end of the specimens so that damage due to spark erosion could be removed. After final polishing, in 25% sulphuric acid in methanol solution, at 5 - 6 volts, the specimens average 6.2 mm in height and 2.8 mm in diameter. Etch pitting techniques and Laue back-reflection photographs were used to ensure that no damage was done to the specimens during sample preparation.

2.4. Etch Pit Studies

In order to understand the behavior of dislocations during slip, etch pitting techniques were used to observe edge and screw dislocation effects by producing the appropriate etching surfaces. The screw surface was cut so that dislocations emerging parallel to it would have a Burger's vector that was parallel to the dislocation line vector. The adjacent face, 90° to it, was cut so that the dislocations coming out parallel to that surface would have a Burger's vector perpendicular to the dislocation line vector. This was the edge surface. One would now be able to observe the two different types of dislocations on each face. For purposes of convenience, surfaces were designated as E (edge) and S (screw) surfaces as shown in Fig. 1.

Symmetric (100) and (110) faces of type A crystals were found by Laue back-reflection photographs and produced by grinding off ~0.015 mm per pass, and electropolishing. The primary slip vector $a/2[1\bar{1}1]$ is perpendicular to the direction [110] and parallel to the direction [100]. (This can be proved easily by performing the dot products between these vectors.) Thus, it is parallel to plane (110) and perpendicular to plane (100), where the former is the S surface, while the latter is the E surface. Edge and screw dislocation motion and generation during microyield would be observed by etching these surfaces.

Etch pitting techniques used by previous investigators (15-17) were studied and tested. It was desirable to choose an etchant that would etch both (100) and (110) type surfaces. 12% sulphuric acid and 26% hydrochloric acid in methanol solution was found to etch both surfaces electrolytically at a voltage of 2 - 3 volts. To ascertain the amount of etching time required and to assure that all dislocations were revealed, preliminary tests were made and the number of pits versus etching time was plotted for both E and S surfaces.

2.5. Compression Testing System

The present experimental set-up is shown schematically in Fig. 3. Two diametrically opposed

LVDT transducers were utilized as displacement gages. Their signals were fed into the A and B inputs of a zero suppression input module of a Daytronic amplifier and were summed and transmitted into the X channel of a Moseley XY recorder. The LVDT gages were calibrated by using micrometers which displaced the transducer cores in controlled amounts.

A ball and push-rod with coupler were used for loading the specimen seated between two tungsten carbide plates which were ground flat and parallel to within ±0.0025 mm over their 25.4 mm diameters. The applied axial load signal obtained from the electronic system of the Instron TT-DM Universal Testing Machine was fed into the Y channel of the XY Moseley recorder. Load calibrations were performed by using calibration weights and the Instron's internal electronic signal for the appropriate load cells used. Load and displacement calibrations were made before and after each test. The microstrain recording system is shown schematically in Fig. 4.

A prestress ~ 0.02 kg/mm^2 was applied on the test specimen after load calibrations. The displacement gages were nulled and adjusted to obtain a suitable sensitivity range. At the maximum sensitivity used, 1 cm of chart on the Y axis corresponded to a stress of 0.05 kg/mm^2, and 1 cm of chart on the X axis corresponded to a strain of 2x10^{-6}mm/mm for the usual specimen size. An open dewar filled with liquid nitrogen was used for low temperature testing. Load-unload experiments were performed at 77°K and 298°K. Some of the samples were etched before and after straining and the distribution of dislocations were compared with respect to temperature dependence, interstitial content, magnitude of plastic strain, and edge-screw behavior. The generation and mobility of both edge and screw dislocations were related to microstrain results and factors that impede plastic relaxations were explored.

It had been indicated that compression microstrain results obtained by using an LVDT transducer (4) did not agree with tension experiments using a capacitance transducer. Later reports (18,19) showed that this was not true. The apparent disagreement in compression and tension data was eliminated in this investigation by using two, instead of one, LVDT transducers that were diametrically opposed and their signals added before being transmitted to an XY recorder.

2.6. Displacement Calibration

Displacement calibrations are essential in compression experiments although hardly necessary in tension experiments. For compression testing, there is no difficulty calibrating the transducer absolute displacements. The difficulty arises when relating the transducer core displacements to the actual sample displacement on a one-to-one basis. In tension, the transducers measure displacements as directly coupled to the gage section, whereas in compression, transducers measure the displacement of two compression plates which includes the relaxations in the compression plates, ball bearing joint, push rod and coupler, and even the load measuring cell itself. These must be taken into account when measuring true sample displacement during compression testing while not necessary in tension. Without this kind of careful calibration, it is very easy to assume displacements in the sample to be much much different from what they are in actuality as due to defect motions within the sample.

In this experiment, load-unload runs were performed on polycrystalline tungsten with a grain size of 100μ. Tungsten had been shown to be isotropic (4), so the problem of texture need not be considered. Similar tests were made by compressing the two tungsten carbide plates with no specimen between them. The results obtained were compared to their known elastic moduli.

§3. RESULTS AND DISCUSSION

Comparisons of results obtained for molybdenum crystals of various purities will be made, as stated above. In order to achieve this, techniques are necessary in purifying these specimens and controlling the levels of impurities in them. Section 3.1 explains how interstitial impurity levels are controlled, while section 3.2 deals with the etch pit results obtained by etching edge and screw surfaces. Determination of modulus defect and mechanical data extracted from compression testing loops are presented in sections 3.3 and 3.4, respectively. Finally, obstacles to dislocation motion will be discussed in section 3.5.

3.1. Control of Interstitial Impurity Levels

An electron beam furnace in an ultra-high vacuum chamber was used to purify and reduce the interstitial content of molybdenum single crystals. Previous studies (20) showed that both nitrogen degassing and engassing were controlled by a simple first order diffusion process. At equilibrium, the concentration of nitrogen in molybdenum, c_N, in atomic percent, is given by (20):-

$$\log c_N = \tfrac{1}{2}\log p_{N_2} - 0.52 - 4940/T \qquad [1]$$

where p_{N_2} is the partial pressure of nitrogen gas, N_2, in torr, and T is the absolute temperature in $^{\circ}$K.

Although oxygen engassing is also diffusion controlled, degassing of oxygen is more complicated. According to Fromm (20), oxygen diffuses to the metal surface during degassing and forms an oxide with the metal. The volatile metal oxide must then be evaporated from the surface of the oxygen solid solution. Metal loss due to oxide formation and evaporation is dependent on the degassing temperature and oxygen partial pressure at steady state (20). This process is surface limited. From thermodynamic data (21), the formation of stable molybdenum oxides above 1275°K is governed by the following equations:-

$$<MoO_2 \;=\; <Mo> + \;(O_2):\; \Delta G_T = 140{,}100 + 4.6T\log T - 55.8T \text{ cal/mole} \qquad [2]$$

$$<MoO_3 \;=\; <MoO_2> + \tfrac{1}{2}(O_2):\; \Delta G_T = 38{,}700 - 19.6T \text{ cal/mole} \qquad [3]$$

Thus, thermal energy must be supplied for the oxygen-metal reaction to take place, and an addition heat of reaction is required to strip the oxides from the metal surface.

Preliminary tests were used to produce intermediate impurity levels. EBZR molybdenum single crystals were outgassed at 2273°K, in a total base pressure of 10^{-8} torr, for 50 hours. This reduced the nitrogen content by nearly 50% (from 42 to 20 ppm), while little reduction was shown in the oxygen level (98 to 96 ppm). This proved Fromm's statement that oxygen degassing was surface limited instead of diffusion controlled like nitrogen degassing. Moreover, it was possible to decrease the nitrogen content while retaining the oxygen impurities. When the oxygen level had to be reduced also, a higher degassing temperature was employed.

Three-pass EBZR single crystals of type A molybdenum were outgassed at 2673°K in a total base pressure of 5×10^{-9} torr at equilibrium. The effectiveness of the degassing process was controlled by performing mass scans at periodic intervals during outgassing. Fig. 5 shows the variation in the partial pressures of the gases at the beginning, the end, and other stages of degassing. Note the significant decrease in height of all the peaks. Due to the complexity involved in oxygen degassing, special attention was paid in monitoring the oxygen, O_2^+, peak. Its variation with degassing time is shown in Fig. 6. The O_2^+ partial pressure decreased by more than two orders of magnitude from $\sim 10^{-7}$ to $7\text{x}10^{-10}$ torr after sixty hours of outgassing. Although a steady-state equation for the Mo-O system has not been established due to insufficient data (22), it can be deduced that the oxygen concentration has been reduced by at least an order of magnitude to ~10 ppm, since the concentration, $c_O \sim (p_{O_2})^{\frac{1}{2}}$, and p_{O_2} was reduced by more than two orders of magnitude. This was confirmed by vacuum fusion analysis to be <10 ppm.

Variation of the N_2^+ peak with degassing time is shown in Fig. 7. A similar decrease in the N_2^+ partial pressure was observed. Using Fromm's equation (20) for the Mo-N system, the nitrogen concentration can be calculated. At the end of degassing, the nitrogen partial pressure was $<10^{-9}$ torr. From Fromm (20):-

$$\log c_N = \tfrac{1}{2}\log p_{N_2} - 0.52 - 4940/T. \qquad [1]$$

At 2673°K, for $p_{N_2} = 10^{-9}$ torr, the concentration of nitrogen in molybdenum is $<10^{-3}$ ppm by weight. Vacuum fusion analysis confirmed the nitrogen content to be <1 ppm. The concentrations of O and N interstitial impurities in the test specimens, verified by vacuum fusion analyses, are shown in Table I. It can be seen that the oxygen content of outgassed type A specimens reduced from 98 to 10 ppm, while the nitrogen concentration decreased from 42 to <1 ppm. Outgassing was stopped after sixty hours since mass scans showed no further reduction in peak levels during the last ten hours of degassing.

The goal in preparing samples with various interstitial purity contents has been achieved. Specimens with high oxygen and nitrogen contents, high oxygen and intermediate nitrogen levels, and low oxygen and nitrogen impurities, were produced with success. These three types of crystals will be used to observe how oxygen and nitrogen impurities affect the dislocation dynamics of BCC molybdenum.

TABLE I

Interstitial Impurity Content*

Specimen Type#	O (ppm)	N (ppm)
A-A	98	42
A-D	<10	<1
B-D	96	20

* Impurity levels were determined by vacuum fusion analyses.

\# Crystals are denoted by the crystal orientation (A=<110>, B=<111>) - processing treatment (A=as grown, using EBZR, D=EBZR+UHV outgassing)

3.2. Etch Pitting Techniques

In order to study the dislocation dynamics resulting from impurity-dislocation interaction, it is necessary to employ etch pitting techniques. It has been found that both (100) and (110) surfaces of the specimens respond best and most consistently when etched electrolytically in a solution of 12% sulphuric acid and 26% hydrochoric acid in methanol solution. For convenience, the same solution was used for electropolishing at a voltage of 7 - 8 volts. After electropolishing for one to two minutes, the voltage was reduced to 2 - 3 volts for etching. The amount of etching time required must be determined carefully. The number of pits increases with time of etching until a maximum is reached, after which the pits will only grow in size. Certain specific areas of the (100) and (110) surfaces were observed using optical metallography. Their etch pit densities were found as a function of etching time until no further changes took place. The typical response for sample A-8-A is shown graphically in Fig. 8. After 60 sec, both surfaces showed no further increase in the number of pits. Thus, all specimens used for etch pit observations were etched for 60 - 65 sec before and after straining. The assurance that the etch pit density remains constant after 60 sec of etching is extremely important because any increase in the number of pits detected after straining can now be attributed solely to mechanical deformation and not the increased response from prolonged etching.

The etch pit densities of as-grown and outgassed specimens are given in Table II. A reduction of ~50% in etch pit density results after 60 hr of ultra-high vacuum degassing. This is true for both E and S surfaces. A direct one-to-one correlation between etch pit density and dislocation density is seldom found for all etchants. After extensive research, Prekel and Lawley (15) reported that only the $\{421\}$ planes gave a one-to-one correspondence between etch pits and dislocations when etched with dilute Mirakami's solution.

In this investigation, the absolute number of dislocations present is not of prime importance.

TABLE II

Dislocation Etch Pit Densities

Specimen*	Plane	Density (cm^{-2})
A-6-A	(100) (110)	6.4×10^5 1.6×10^5
A-8-A	(100) (110)	7.1×10^5 1.3×10^5
A-1-D	(100) (110)	2.2×10^5 7.4×10^4
A-2-D	(100) (110)	2.7×10^5 6.9×10^4

*Original crystals are denoted by the crystal type (A, B, C) - processing treatment (A = as grown, using EBZR, D = EBZR + UHV degassing). The number in the middle denotes the section cut from the original crystal.

Rather, the relative number of dislocations generated and moved during compression testing was to be observed in detail. The etchant chosen is capable of etching both (100) and (110) type surfaces. Moreover, freshly generated dislocations were revealed effectively and consistently.

3.3. Determination of Modulus Defect

As stated earlier, in section 2.6, it is essential to perform displacement calibrations in order to obtain a one-to-one correspondence between compression plate displacements and true specimen displacements. Modulus data in this work were standardized by using a large grain isotropic tungsten polycrystal of known modulus and the machine stiffness was determined by using this set of standard samples. In addition, the linearity of response from the machine was checked out by compressing the tungsten carbide plates without any sample between them. It is necessary to ensure that the machine behaves linearly within the load range used for molybdenum testing because of possible deflections in the load cell, push rod, ball bearing and various coupling assemblies. Fig. 9 shows the machine stiffness constant as a function of load which is level to loads of 12 kg. Beyond this point, the machine starts behaving in a non-linear manner. Such deviations from linearity is probably due to machine stiffness effects. It must be noted, that for this assmebly, the machine has a characteristic range over which its stiffness is independent of load for strain sensitivities in the range ~$1x10^{-6}$. (In the usual sense, for sentivities ~10^{-4}, this type of machine would be considered stiff to its maximum designed load.) Moreover, the machine exhibits zero point repeatability up to loads of at least 20 kg (higher loads are not necessary for the present work). This was also checked with the standard isotropic tungsten sample and load independence was observed. The machine modulus was then calibrated against these samples. All other moduli in this thesis were standardized similarly.

Initial moduli values of unstrained specimens of various orientations and purity levels were measured. Table III shows the typical initial relaxed moduli for different specimens used. The measured relaxed moduli, E_R, were compared to the theoretical values, E_D, obtained from acoustic measurements of the compliances, S_{ij}'s (23). For cubic crystals, the elastic moduli in the three low index orientations are given by:-

$$E_{100}^{-1} = S_{11} \qquad [4]$$

$$E_{110}^{-1} = S_{11} - 2/4(S_{11} - S_{12} - \tfrac{1}{2}S_{44}) \qquad [5]$$

$$E_{111}^{-1} = S_{11} - 2/3(S_{11} - S_{12} - \tfrac{1}{2}S_{44}) \qquad [6]$$

By comparing the measured moduli values to the dynamic moduli, a certain reduction can be observed. This set of data is consistent with the measured moduli values of tungsten, molybdenum and iron, as measured by Meakin (4), which displayed deviations within the range of ~-10 to 2.5%. However, some crystals used in this investigation were UHV outgassed in addition to EBZR, thus giving a higher % deviation. The reasons for this will be discussed in detail below when the effects of purification , possible obstacles to dislocation movement, and etch pit studies are also correlated to relaxed modulus observations. The measured moduli of the outgassed specimens deviated by ~13% from the dynamic modulus,

TABLE III

Measured Moduli Values (as corrected)

Specimen	Relaxed Modulus $E_R \times 10^{-3}$ kg/mm^2	Dynamic Modulus $E_D \times 10^{-3}$ kg/mm^2	% Deviation
A-8-A	29.15	31.04	- 6.0
A-1-D	26.92	31.04	-13.2
A-3-D	27.10	31.04	-13.0
B-2-D	26.98	29.59	- 8.8
C-5-A	35.47	36.42	- 2.6

while only a 6% deviation was observed for the as-grown sample taken from the same initial crystal.

The reduction in measured moduli values is known as modulus defect. This is due to non-linear components responding to the stress field of the sample and has been attributed to dislocation bowing in many microstrain experiments (9, 24). Strain amplitudes used in compression testing are large compared to usual acoustic measurements and a uniform stress is applied to the solid where every dislocation should respond to this stress. Only a small part of the sample is excited at any one time during an acoustic experiment when pulses are sent into the sample. Also, there is no acoustic beam divergence for mechanical testing since the stress applied is uniform from edge to edge if the sample is properly aligned, and did not bulge in any non-uniform way. Mathematically, the modulus defect is defined as:-

$$\text{Modulus defect} = (E_D - E_R)/E_D = \Delta E/E_D \quad [7]$$

where E_R is the measured relaxed modulus and E_D is the dynamic modulus obtained from acoustic measurements.

The modulus defect should change when more and more dislocations are brokenaway. The modulus defect for two different types of samples were studied, at 298^{o}K and 77^{o}K, as a function of stress amplitude, but with totally reversible strain to determine whether more and more loops were brokenaway from pins instead of only kink activated as the stress amplitude was increased. As can be seen from Fig. 10, both outgassed and as-grown crystals did indeed show a shift in relaxed modulus which decreased with increasing stress amplitude, and finally saturated at $\sim 1.26 \times 10^{4}$ kg/mm^{2} once some permanent strain was observed. This was not taken to extremely large strains, but it did show that eventually enough loops were brokenaway. When all the easy loops were brokenaway from impurity pins, the modulus defect saturated for that given prestrain. The modulus defect for these two crystals are plotted as a function of stress in Fig. 11. For small stress amplitudes, outgassed samples have a much higher modulus defect than as-grown specimens. This is due to a fewer number of pins present in the crystal lattice thus enabling easier and more profuse dislocation breakaway. When plastic deformation occurs, both specimens saturated at the same modulus defect level because all the easy loops have brokenaway in both cases. Similar stress amplitude dependences were observed for the moduli values of outgassed and as-grown specimens at 77°K.

As an intermediate purity level comparison, the modulus defect observed in an outgassed type B molybdenum specimen is shown in Fig. 11 on the same plot for type A specimens. Type B-D specimens had approximately the same level of oxygen impurities and ~50% reduction in the nitrogen content when compared to type A-A samples, thus they serve to act as an intermediate purity level comparison between as-grown and outgassed crystals. The absolute magnitudes of E_R cannot be compared because of anisotropy, since type A and type B crystals have different orientations. Instead, their modulus defect changes were observed, therefore taking into account the initial values of E_D due to crystal orientation. It can be seen that the type B-D specimen had a higher modulus defect than the as-grown sample but a lower modulus defect than the outgassed crystal,until saturation occurs at higher plastic prestrains. Hence, both oxygen and nitrogen interstitials act as pins to obstruct dislocation breakaway and the effect of oxygen impurities alone is less pronounced than when both interstitials are present. The modulus defect observed for type C specimens is much lower, as can be seen from Table III. Although type C crystals are EBZR, only one zone-pass was performed, as opposed to three zone-passes for type A and B crystals. Thus, higher substitutional and interstitial impurities are present and more impedence to dislocation motion is evident in the higher relaxed modulus value measured. The dislocation densities of all crystals are of the same order of magnitude, so the above-mentioned effect could not be due to dislocation density changes.

3.4. Microstrain Observations

Some typical load-unload traces are shown in Fig. 12. Mechanical hysteresis loops obtained are not parallelograms, as reported by Meakin (4), but they are lenticular and similar to those found by McMahon et al (21). This difference is due to the installation of two diametrically opposed LVDT transducers whose signals are added before being transmitted to the XY recorder. Bending in the compression plates and other components of the load train can be compensated by using two LVDT's instead of one. The loops produced are similar to those from capacitance transducers (25). It should be noticed that the initial slopes of these traces decrease with increasing stress amplitude. This shift in slope indicates that more and more of the network is contributing to dislocation bowing as stress amplitude is increased although there is completely reversible strain within sensitivity of $\sim 2\times10^{-7}$. At sufficiently low stresses, the modulus defect is small, this is in agreement with Meakin's analysis (4). Initially, dislocation bowing is difficult, hence the modulus is high. As the stress amplitude is increased, dislocations are unpinned, and the magnitude of E_R is decreased. However, when a critical stress level is reached, E_R remains more or less constant and saturation occurs as all the easy loops have brokenaway and permanent plastic strain is then observed.

The magnitudes of the elastic limit, σ_E (stress amplitude at which the load-unload trace deviates from a straight line) and the anelastic limit, σ_A (stress amplitude at which the hysteresis loop opens irreversibly) of type A crystals are shown in Table IV. At 298°K, σ_A of the as-grown specimen is more than double that of the outgassed sample while σ_E is also reduced significantly by outgassing. Similar results are observed for the low temperature test. This set of data further confirms that dislocation motion and unpinning are hindered by interstitial impurities. Moreover, dislocation unpinning is thermally assisted. For the same temperature reduction, the as-grown specimen exhibits a larger increase in σ_E (4.2%) and σ_A(5.2%) as compared to the 3.0% increase in σ_E and 4.4% increase in σ_A of the outgassed sample. At lower temperatures, thermal assistance is reduced, thus additional mechanical stress must be applied for dislocation breakaway. This is illustrated by the higher σ_E and σ_A values at 77°K.

3.5. Obstacles to Dislocation Motion

It has been mentioned in sections 3.3 and 3.4

TABLE IV

Observed Elastic and Anelastic Limits

Specimen	Temp. °K	σ_E, kg/mm^2	σ_A, kg/mm^2
A-8-A	298	0.240	2.680
A-6-A	77	0.250	2.820
A-1-D	298	0.160	1.360
A-2-D	77	0.165	1.420

that the slope of the stress-strain curve shifts with stress amplitude. This gives some insight on the breakaway process for dislocation bowing between strong nodes in a way discussed by the Granato-Lucke model (26). A decrease in modulus is caused by the breakaway of more and more dislocation loops. Some estimate on the number and length of loops would be helpful in identifying the type of pinning mechanism involved. Several physical assumptions can be made: 1) that all dislocations are unpinned, 2) that some are pinned more strongly than others, 3) that the nature of pinning is due to random interaction or supersaturation pf solutes, and, 4) that the modulus defect is solely due to some kink mechanism and not interstitial pinning. (Forest mechanism is not considered important in BCC metals (27, 28)). The last assumption can be eliminated by the fact that outgassed and as grown crystals have dislocation densities that are different by a factor of two, for a reduction in oxygen content from 98 to 10 ppm and a decrease in nitrogen content from 42 to <<1 ppm. Moreover, at low stresses, outgassed specimens have a much higher modulus defect than as-grown samples, as mentioned in the preceeding sections. Although kink mechanisms are not solely responsible for modulus defect observations, the internal friction of the BCC metal may be dependent on some type of kink mechanism. The first assumption can be disproved by etch pit studies. Only a certain percentage of pits was observed to move during straining and some were retrapped. Retrapping of dislocations has also been observed for tungsten (29). Thus, not all of the dislocations are completely unpinned.

In order to determine the pinning mechanisms controlling initial dislocation movement, it is applicable to estimate the breakaway energy by using the Teutonico-Granato-Lucke model (30). The binding energy, U_o, required for mechanical breakaway is given by:-

$$U_o = \sigma_o b^2 l \qquad [8]$$

where σ_o is the breakaway stress, b is the Burger's vector and l is the distance between pinning points. When saturation is reached in the amplitude dependence of the modulus defect, as shown in Fig. 11, all the loops that will breakaway from weak solute pins must

must have brokenaway. That stress level will be taken as σ_O, the breakaway stress required for unpinning of all the easy sources. For example, if oxygen is the pinning agent, various assumptions can be made as to where the oxygen is in the lattice. The actual location of oxygen on a dislocation site in a bulk specimen like this has never been found, so an elimination process of the different possibilities must be made. Perhaps further development in FIM studies or other more sophisticated experimental techniques will give a better idea of the saturation ratios between the lattice and the dislocation line.

Assuming oxygen to be fully responsible for pinning in the as-grown samples, for a random distribution of 98 ppm by weight of oxygen, the binding energy is found to be 0.47×10^{-1} eV. If all the oxygen molecules are situated on dislocation lines (i.e. full saturation), the value of U_O is 0.47×10^{-8} eV. (Sample calculations of U_O are shown in the Appendix.) The reason for the large decrease in binding energy found for the case when all the oxygen molecules are on dislocation lines is explained by the Teutonico-Granato-Lucke model (30). As the loop length decreases, the stress should have risen for breakaway but in the present calculations of U_o, the stress is taken to be constant while the loop length is allowed to be the free variable, thus U_o would decrease with decreasing length l.

Comparison of the binding energies calculated above with the value of ~0.1 eV, determined by Gibala et al (31), from internal friction measurements in the Mo-O system, indicates that the model of nearly random interstitial solute pinning is consistent with the observed results. The longest distance between pits, found from etch pit studies, is 0.005 cm. For a binding energy ~0.1 eV, as reported by Gibala et al (31) the value of l should be $8.0\text{x}10^{-4}$ cm. Thus, each loop may have ~8 pinning points, and the number of oxygen molecules taking part in the initial breakaway is $8 - 50\text{x}10^{8}$ cm^{-3} compared to the total concentration of $1.88\text{x}10^{19}$ cm^{-3}. Therefore, unpinning was achieved by breakaway of all the weak solutes, which is only a small fraction of the interstitial impurity content, and further shows that not all the dislocations are unpinned.

Typical etched (100), E, and (110), S, surfaces of as-grown and outgassed type A specimens photographed before and after straining are shown in Figs. 13 - 16. The number of pits generated and moved during mechanical deformation is compared to the original etch pit distribution before testing. The variations of etch pit density with plastic strain for various specimens are shown graphically in Fig. 17. Both E and S surfaces displayed an increase in etch pit density with increase in plastic strain. A similar behavior of stress dependence is shown in Fig. 18. Although etch pit densities of both E and S surfaces increase with stress and strain, plots for E surfaces are different in slopes than those of S surfaces. This shows that the number of edge dislocations increases tremendously with the first sign of plastic strain while screw generation is insignificant. For higher values of stress and strain, exhaustion of edge dislocation generation is observed, but a much higher number of screw dislocations is produced. The edge dislocations are exhausted, while screw dislocations catch up in number. Thus, in the microstrain region, edge dislocations are predominant in controlling the flow stress until exhaustion occurs.

The percentage of dislocations generated and moved in the outgassed specimens are more, in all cases, than in the as-grown samples. This shows that interstitial impurities, such as oxygen and nitrogen, act as dislocation pinning sources, thus strengthening the metal. Less dislocations are generated and less movement is observed for the crystal with a higher interstitial content although these specimens are cut from one original crystal and are of comparable initial dislocation densities. The temperature dependence of this interaction is demonstrated by the lower number of dislocations being generated at 77°K. Similarly, fewer dislocations have moved because thermal assistance in dislocation unpinning is less effective at 77°K. Dislocation repinning is observed frequently (56%) in the as-grown samples, but very seldom (7%) noticed in the outgassed case. Unpinned dislocations of the as-grown samples are retrapped by the interstitial impurities.

The plastic strain, ε_p, can be expressed in terms of the number of dislocations, N, the burgers vector, b, and the dislocation length, l, by the plastic strain law:-

$$\varepsilon_p = Nbl \qquad [9a]$$

$$\dot{\varepsilon}_p = Nbl + Nb\bar{v} \qquad [9b]$$

From this investigation, it is observed that both dislocation generation and motion aid in producing plastic strain. Average dislocation velocities are calculated by dividing the farthest distance moved by dislocations from their original positions in the unstrained specimen by the loading time. Loading times were measured by load-time curves that were plotted by a two-channel recorder during load-unload cycles of mechanical testing. Loading times are in the order of ~15 sec. The calculated values of dislocation velocities, v, are tabulated in Table V, and are shown graphically as functions of plastic strain and stress amplitude, in Figs. 19 and 20 respectively. Values of v reported in the literature (32) range from $\sim 10^{-5}$ to 10^{-3} cm/sec for resolved shear stresses ~0-2 kg/mm^2.

TABLE V

Observation of Dislocation Velocities

Specimen	Temp. $^{\circ}$K	Surface	τ^*, kg/mm^2	Calculated v, cm/sec	Reported v, (32) cm/sec
A-8-A	298	E S	1.64	1.1x10^{-3} 4.0x10^{-5}	$\sim$5.0x10^{-4} -
A-6-A	77	E S	1.72	1.8x10^{-4} 3.2x10^{-6}	- -
A-1-D	298	E S	1.58	3.0x10^{-3} 5.0x10^{-5}	$\sim$5.0x10^{-4} -
A-2-D	77	E S	1.60	2.3x10^{-4} 4.4x10^{-6}	- -

For type A crystals, the resolved shear stress, $\tau^* \simeq 0.42\sigma$, and the values of v calculated in this investigation compare well to those of Conrad et al (32) for the same τ^*.

It can be seen that velocities of edge dislocations are much higher (by ~2 orders of magnitude) than those of screws at both test temperatures. Also, dislocation velocities, both edge and screw, are faster for outgassed crystals than as-grown samples. This illustrates that interstitial impurities act as dislocation pins and hinder dislocation bowing. When more plastic strain is produced, the velocities of dislocations in both samples have approximately the same magnitude. This occurs when all the easy loops have brokenaway and is consistent with modulus defect observations mentioned in section 3.3. Hence, in the microstrain region, dislocation bowing is governed by the fast movement of edge dislocations which may be pinned by interstitial impurities. Dislocation movement was observed to occur on $\{110\}\langle 111\rangle$ for both E and S surfaces.

§4. CONCLUSION

Oxygen and nitrogen impurity levels in three-pass EBZR molybdenum single crystals have been reduced, from 98 to <10 ppm and 42 to $\ll$1 ppm, respectively, by UHV outgassing. Dislocation densities measured on both the (100), E and (110), S side surfaces of compression samples are reduced ~50% by this purification. Determination of modulus defect shows a 6% reduction for as-grown crystals and a 13% decrease for outgassed samples at low stress levels. The difference in modulus defect is attributed to dislocation pinning by interstitial impurities. When some prestrain is observed at a higher stress level, the modulus defect saturates, and all the easy dislocation loops have brokenaway. Due to impurity pinning, the stress amplitude at which permanent plastic strain is observed, σ_A, and the stress amplitude at the beginning of dislocation bowing, σ_E, are higher for samples of higher interstitial impurity content. At 298°K, σ_A for a typical high interstitial content specimen is more than double that for an UHV purified sample.

Calculations of dislocation loop length, based on the Teutonico-Granato-Lucke model and Gibala's value for U_o, show good agreement for a random solute interaction model with an l value of $\sim 8\times10^{-4}$cm, which is consistent with the etch pit dynamics observed in the present experiments. Additional etch pit observations proved that only a certain fraction, $\lesssim 1\%$, of the grownin dislocations are unpinned. Dislocation velocities on the (100), E and (110), S side surfaces are found to be in the range 10^{-6} to 10^{-3} cm/sec and are functions of plastic strain and stress amplitude. Similar stress and strain dependences are observed in dislocation densities. From comparisons on the anisotropy in generation and motion of dislocations on (100), E and (110), S surfaces, it has been shown that edge dislocations are predominant in the microstrain region. However, as the macrostrain region is approached (i.e., strains 10^{-4}), the grownin edge segments are exhausted and screw dislocations become dominant in dislocation generation and mobility.

REFERENCES

1. Stein, D.F., 1967, Can. J. Phys., 45 1063
2. Lawley, A., Liebmann, W., and Maddin, R., 1961, Acta Met., 9 841
3. Lawley, A., Van den Sype, J., and Maddin, R., 1962, J. Inst. Metals, 91 23
4. Meakin, J.D., 1967, Can. J. Phys., 45 1121
5. Guiu, F., 1969, Scripta Met., 3 449
6. Etemad, B., and Guiu, F., 1974, Scripta Met. 8 931
7. Vitek, V., Perrin, R.C., and Bowen, D.K., 1970, Phil. Mag., 21 1049
8. Koo, R.C., 1963, Acta Met., 11 1083
9. Hartley, C.S., and Wilson, R.J., 1963, Acta Met., 11 835
10. Roberts, J.M., and Brown, N., 1960, Trans. AIME, 218 454
11. Meakin, J.D., and Wilsdorf, H.G.F., 1960, Trans. AIME, 218 745
12. Lawley, A., and Meakin, J.D., 1966, Acta Met., 14 236

13. Meakin, J.D., and Lawley, A., 1966, Acta Met., 14 1854

14. Dralla, J.R., 1973, Ph.D. Dissertation, S.U.N.Y. at Stony Brook

15. Prekel, H.L., and Lawley, A., 1966, Phil. Mag., 14 545

16. King, G.W., and Spretnak, J.W., 1964, Trans. AIME, 230 1481

17. Aust, K.T., and Maddin, R., 1956, Acta Met., 4 632

18. Tomalin, D.S., Pope, D.P., and McMahon Jr., C.J., 1973, Met. Trans., 4 1638

19. Tomalin, D.S., and McMahon Jr., C.J., 1973, Acta Met., 21 1189

20. Fromm, E., 1970, J. Vac. Sci. Tech., 7 no. 6 S100

21. Kubaschewski, O., and Catterall, J.A., 1956, Thermochemical Data of Alloys, pp 168-169, Pergamon Press, London & New York

22. Fromm, E., and Jehn, H., 1972, Met. Trans., 3 1685

23. Hirth, J.P., and Lothe, J., 1968, Theory of Dislocations, pp 761-763, McGraw Hill

24. Dralla, J., and Bilello, J.C., 1970, J. Phys. Chem.

25. Kossowsky, R., and Brown, N., 1966, Acta Met., <u>14</u> 131

26. Granato, A., and Lucke, K., 1956, J.A.P., <u>27</u> 583

27. Seeger, A., and Bohdan, S., 1971, Scripta Met., <u>5</u> 875

28. Chambers, R.H., and Schultz, J., 1962, Acta Met., <u>10</u> 466

29. Tandon, K.N., 1972, Ph.D. Dissertation, S.U.N.Y. at Stony Brook

30. Teutonico, L.J., Granato, A.V., and Lucke, K., 1964, J.A.P., <u>35</u> 220

31. Korenko, M.K., Mitchell, T.E., and Gibala, R., 1974, Acta Met., <u>22</u> 649

32. Prekel, H.L., Lawley, A., and Conrad, H., 1968, Acta Met., <u>16</u> 337

APPENDIX

Sample calculations of the distance between interstitial impurities and the binding energy, U_o, are given below:-

Assuming that oxygen is the impurity responsible for pinning, and for an oxygen content of 98 ppm, since the density of Mo is 10.22 g/cm^3,

$$\text{Weight of oxygen in 1 cm}^3 \text{ of Mo} = 10.22\times 9.8\times 10^{-5} \text{ g}$$
$$= 1\times 10^{-3} \text{ g}$$

$$\text{Avogadro's number,} \quad 32 \text{ g O} = 6.02\times 10^{23} \text{ molecules}$$

Therefore, number of O_2 molecules per unit volume of Mo

$$= 6.02\times 10^{23}\times 10^{-3}/32 \text{ cm}^{-3}$$
$$= 1.88\times 10^{19} \text{ cm}^{-3}$$

If O_2 molecules are randomly distributed throughout crystal,

$$\text{Distance between } O_2 \text{ molecules} = (1.88\times 10^{19})^{-1/3} \text{ cm}$$
$$l = 3.76\times 10^{-7} \text{ cm}$$

$$\text{Binding energy } U_o = \sigma_o b^2 l$$

$$\text{For Mo,} \quad b = 2.73\times 10^{-8} \text{ cm}$$

$$\sigma_o = 2.68 \text{ kg/mm}^2 = 2.68\times 10^2 \text{ kg/cm}^2$$

$$U_o = (2.68\times 10^2)(2.73\times 10^{-8})^2(3.76\times 10^{-7}) \text{ kg-cm}$$
$$= 7.5\times 10^{-20} \text{ kg-cm}$$

$$= 7.5\times10^{-22} \text{ kg-m}$$
$$= 7.4\times10^{-21} \text{ j}$$
$$\text{or,} \quad U_o = 0.47\times10^{-1} \text{ eV}$$

If O_2 molecules are totally on dislocation lines

Dislocation density $= 7.05\times10^{5}$ cm/cm^{3}

Density of O_2 molecules $= 1.88$ molecules/cm^{3}

Therefore, no. of O_2 molecules on a unit length of

dislocation line $= 1.88\times10^{19}/7.05\times10^{5}$ cm^{-1}

$$= 2.66\times10^{13}/\text{cm}$$

Distance between O_2 molecules

$$= (2.66\times10^{13})^{-1} \text{ cm}$$
$$l = 3.75\times10^{-14} \text{ cm}$$

Binding energy $U_o = \sigma_o b^2 l$

$$= (2.68\times10^{2})(2.73\times10^{8})^{2}(3.75\times10^{-14})$$
$$U_o = 0.47\times10^{-8} \text{ eV}$$

Figure 1

Orientation of compression axis of type A crystals. Glide plane, edge (E), and screw (S) surfaces are also shown.

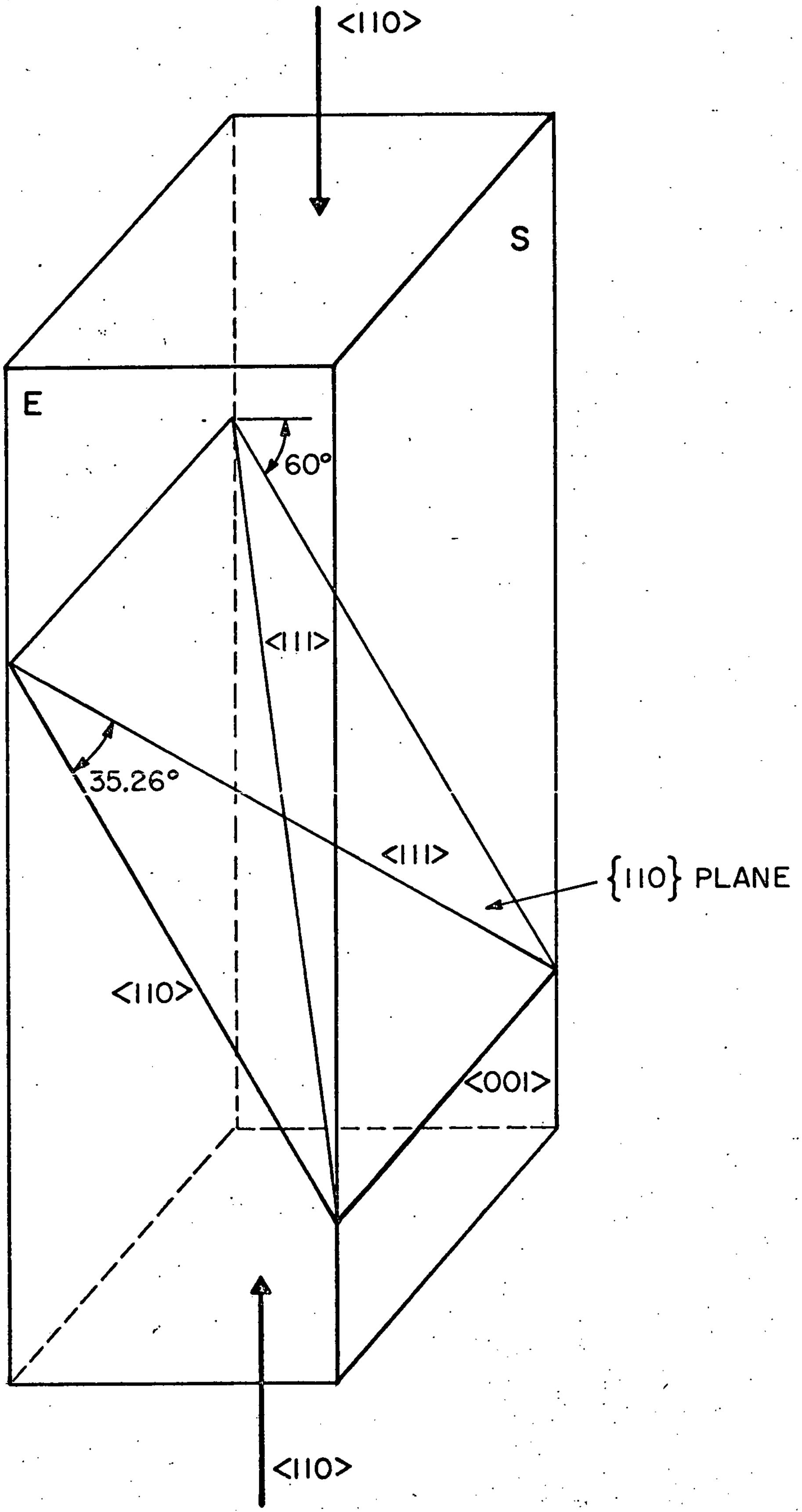

FIGURE 1

Figure 2

(a) Top view of tungsten carbide polishing disk,arrow shows molybdenum specimen held with some crystal bond.

(b) Side view of polishing disk,arrows indicate specimen ends showing on either side.

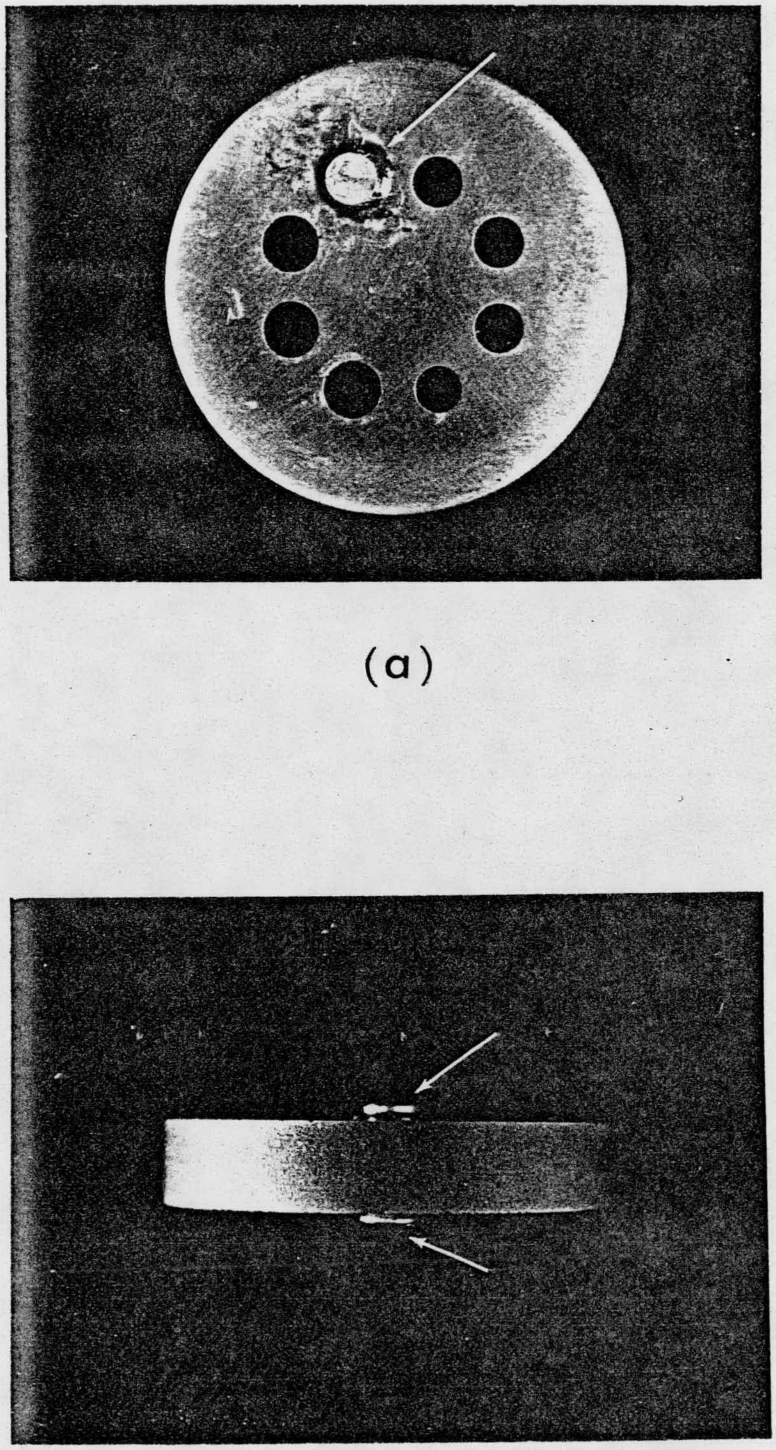

(a)

(b)

FIGURE 2

Figure 3

Schematic of compression plate held to crosshead of Instron testing machine by hollow evacuated cage supports (A). Micrometers (B) are attached to LVDT cores and are used for displacement calibrations. LVDT's (C) are embedded in the stainless steel compression plate and their signals are transmitted to a Daytronic input module. Loading is accomplished via a stainless steel push rod (F), alignment ball (E), stainless steel loading plate (D) and tungsten carbide plates (G). The specimen (S) seats between these carbide plates.

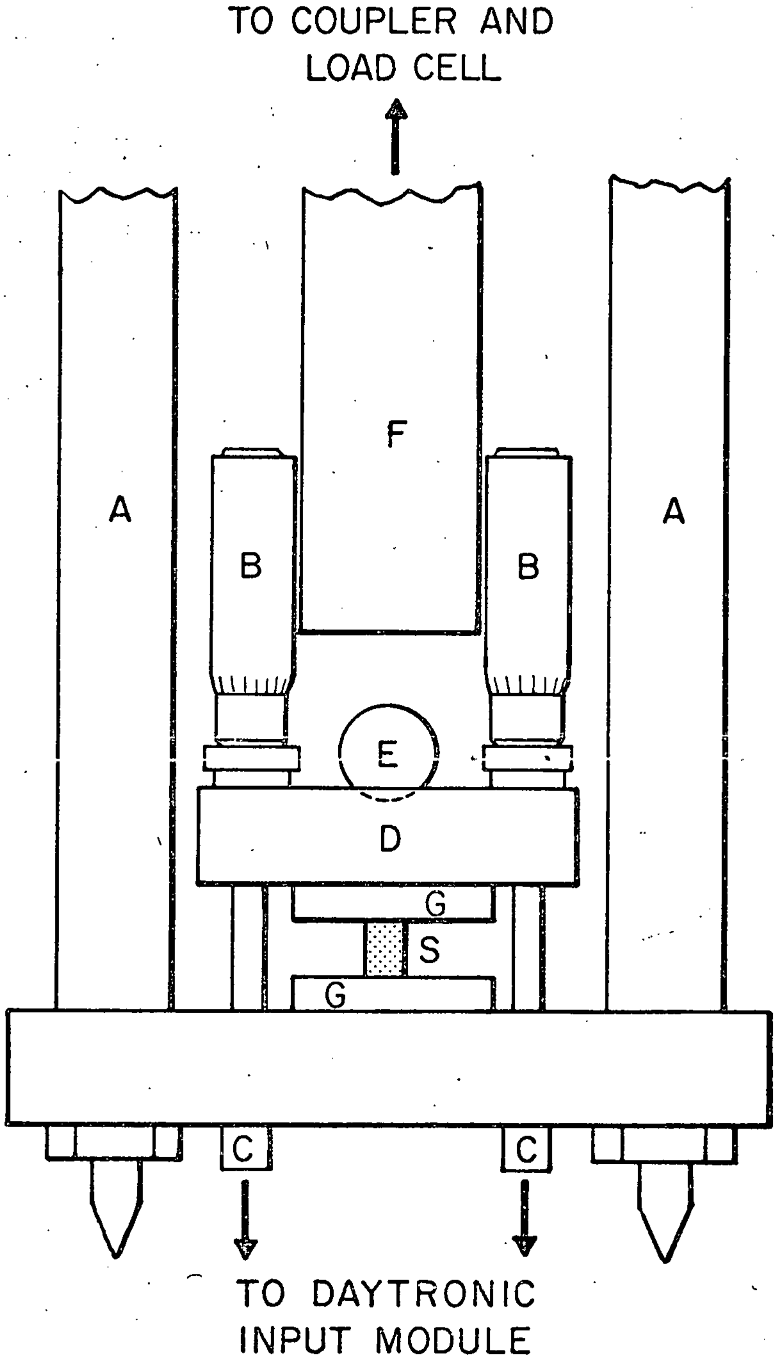
TO COUPLER AND LOAD CELL
F
A
A
B
B
E
D
G
S
G
C
C
TO DAYTRONIC INPUT MODULE

FIGURE 3

Figure 4

Schematic of the microstrain recording system. Load signals from the load cell are amplified in the Instron's internal electronic system and transmitted to the Y channel of a Moseley XY recorder. Displacements are measured by two diametrically opposed LVDT's whose signals are transmitted to a Daytronic input module, summed and relayed to the X channel of the XY recorder.

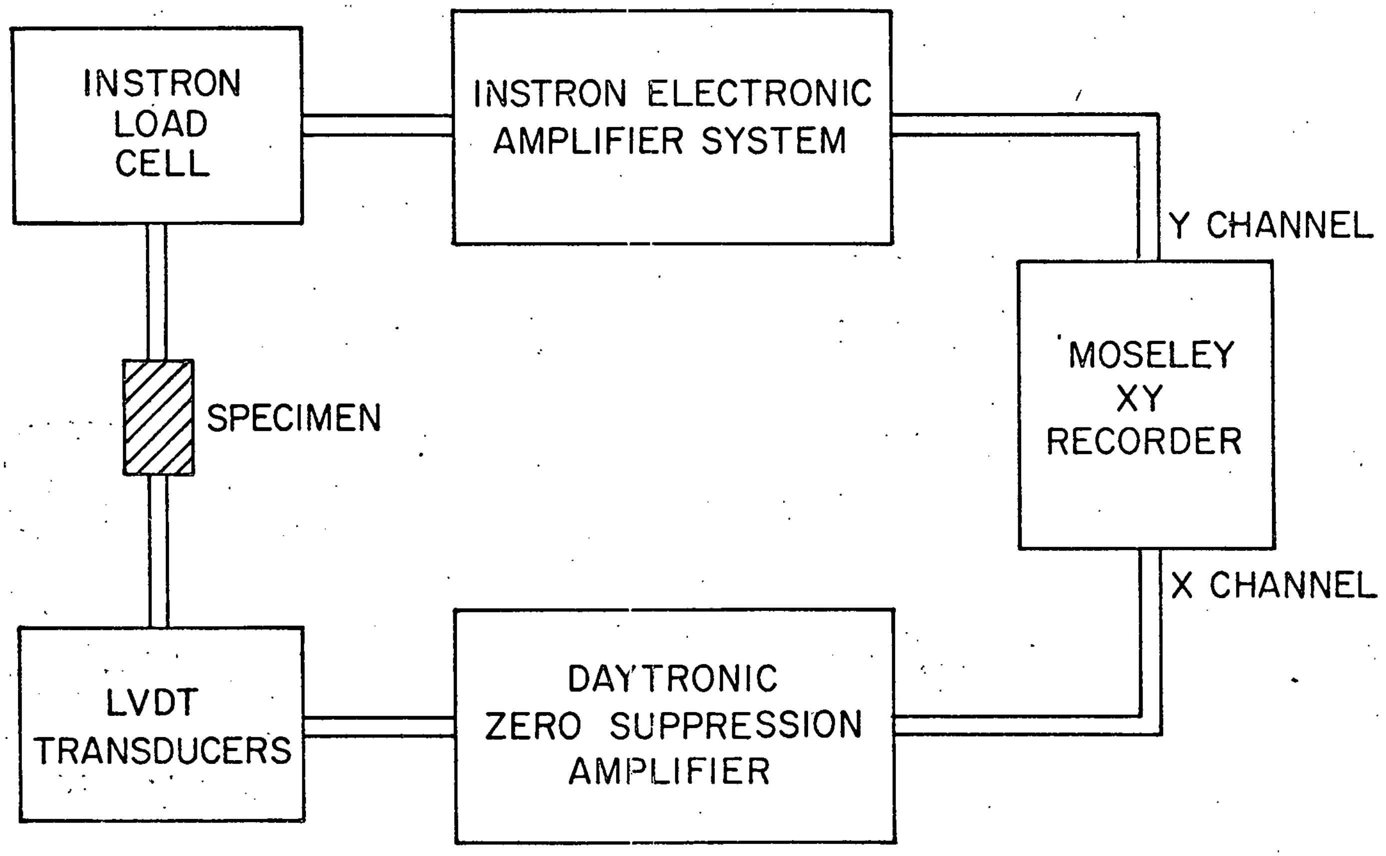
INSTRON LOAD CELL
INSTRON ELECTRONIC AMPLIFIER SYSTEM
Y CHANNEL
MOSELEY XY RECORDER
SPECIMEN
X CHANNEL
LVDT TRANSDUCERS
DAYTRONIC ZERO SUPPRESSION AMPLIFIER

FIGURE 4

Figure 5

Typical mass scans obtained during different stages of UHV outgassing at $2673^{\circ}K$. Note the variation in heights of the O_2^+, N_2^+, and HOH^+ peaks.

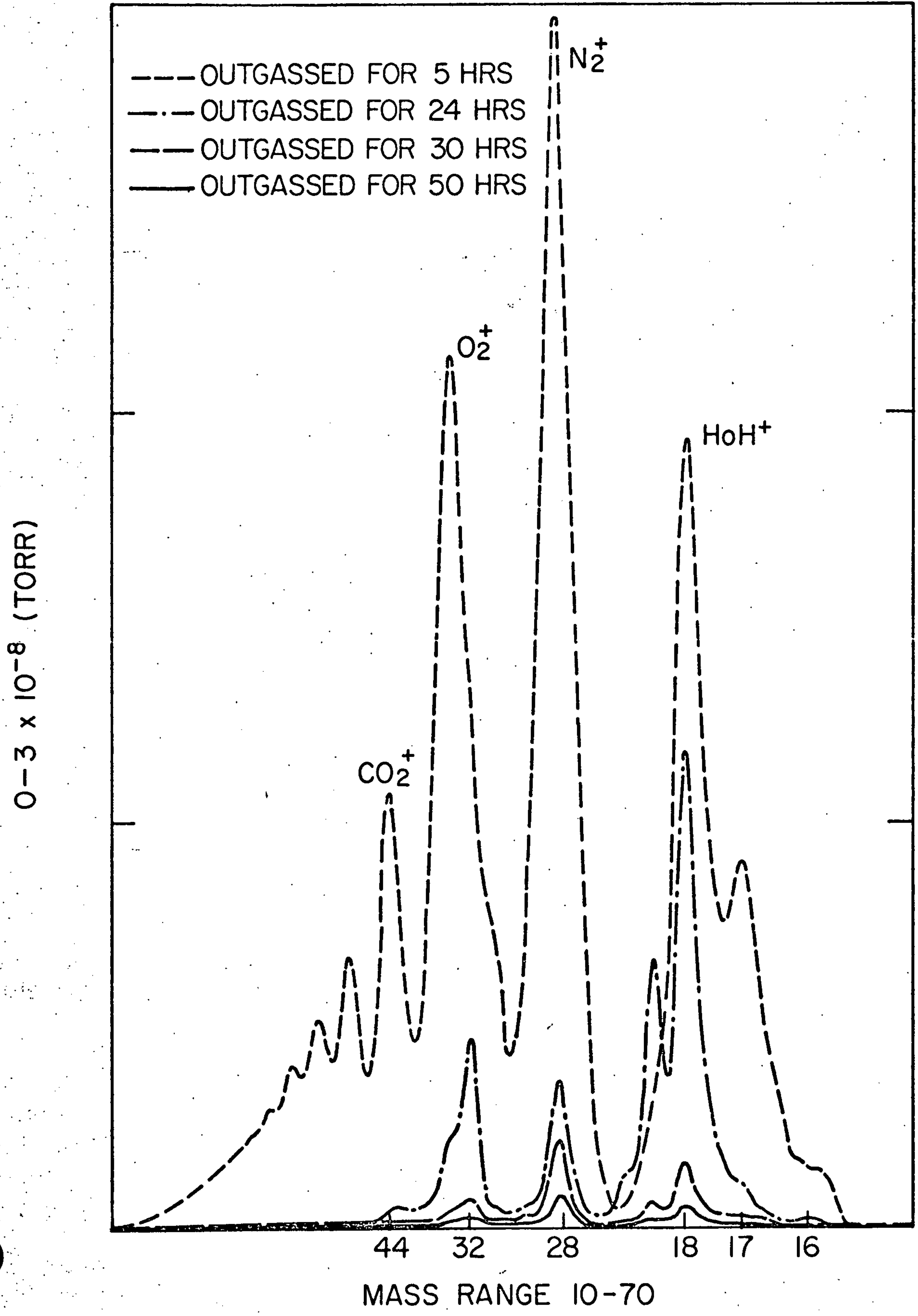
---OUTGASSED FOR 5 HRS
—·—OUTGASSED FOR 24 HRS
— —OUTGASSED FOR 30 HRS
——OUTGASSED FOR 50 HRS
N_2^+
O_2^+
HoH^+
CO_2^+
O-3 x 10^{-8} (TORR)
44
32
28
18
17
16
MASS RANGE 10-70

FIGURE 5

Figure 6

Variation of the O_2^+ partial pressure as a function of total outgassing time. Partial pressures were read from mass scans typical of those shown in Figure 5. Temperature of the electron beam furnace reached 2673°K at 0 hr and furnace was turned off at 60 hr.

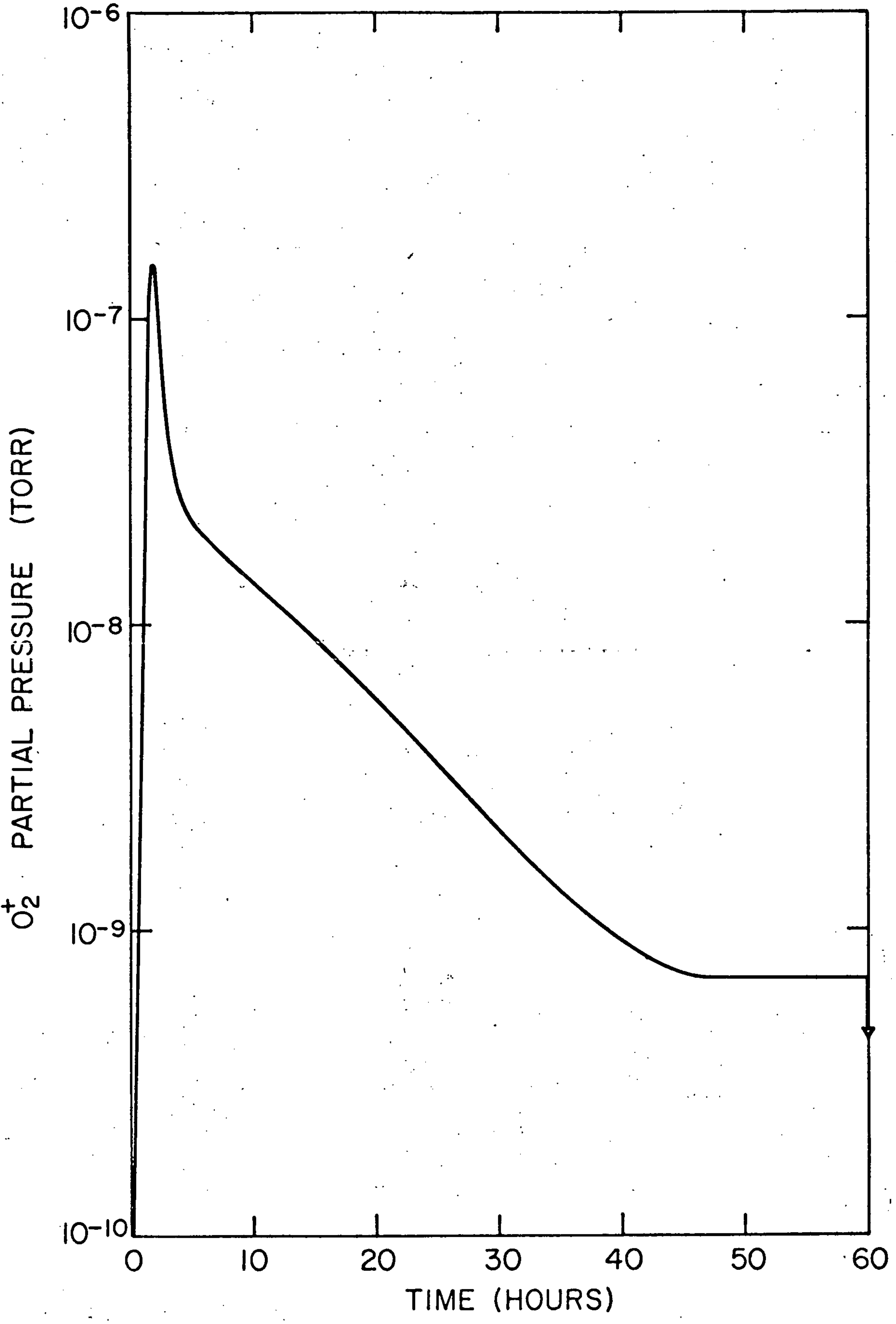
10^{-6}
10^{-7}
10^{-8}
10^{-9}
10^{-10}
O_2^+ PARTIAL PRESSURE (TORR)
0
10
20
30
40
50
60
TIME (HOURS)

FIGURE 6

Figure 7

Variation of the N_2^+ partial pressure as a function of total outgassing time. Partial pressures were read from mass scans typical of those shown in Figure 5. Temperature of the electron beam furnace reached 2673°K at 0 hr and furnace was turned off at 60 hr.

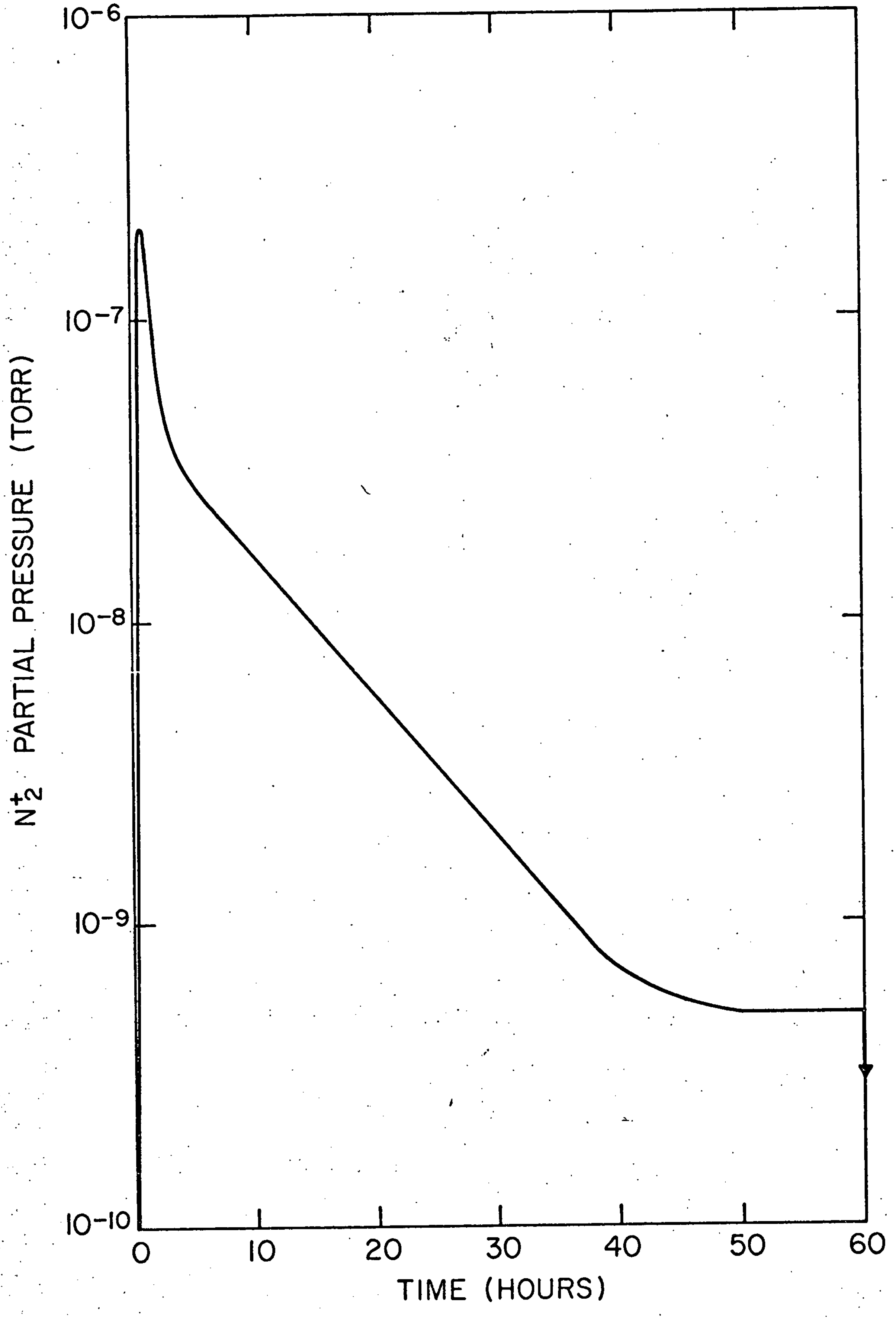
10−6
10−7
10−8
10−9
10−10
N_2^+ PARTIAL PRESSURE (TORR)
0
10
20
30
40
50
60
TIME (HOURS)

FIGURE 7

Figure 8

Typical etch pit density variations with increasing etching time. Response for both (100) and (110) faces are shown.

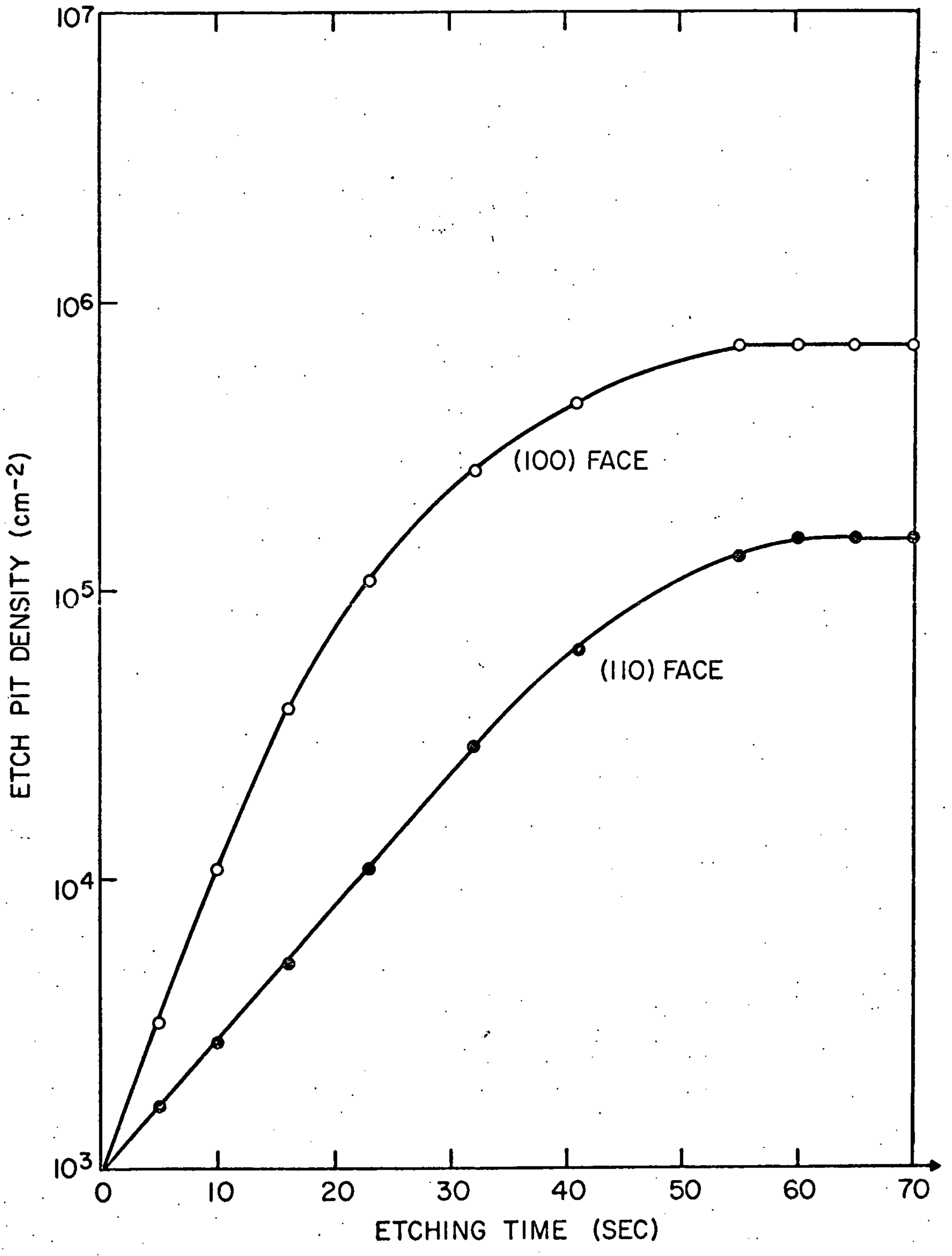

10^7
10^6
10^5
10^4
10^3
ETCH PIT DENSITY (cm^{-2})
(100) FACE
(110) FACE
0
10
20
30
40
50
60
70
ETCHING TIME (SEC)

FIGURE 8

Figure 9

The machine stiffness constant is observed to be linear with increasing load until 12 kg when it starts to deviate from linearity. No mechanical data reported in this thesis is taken beyond this load.

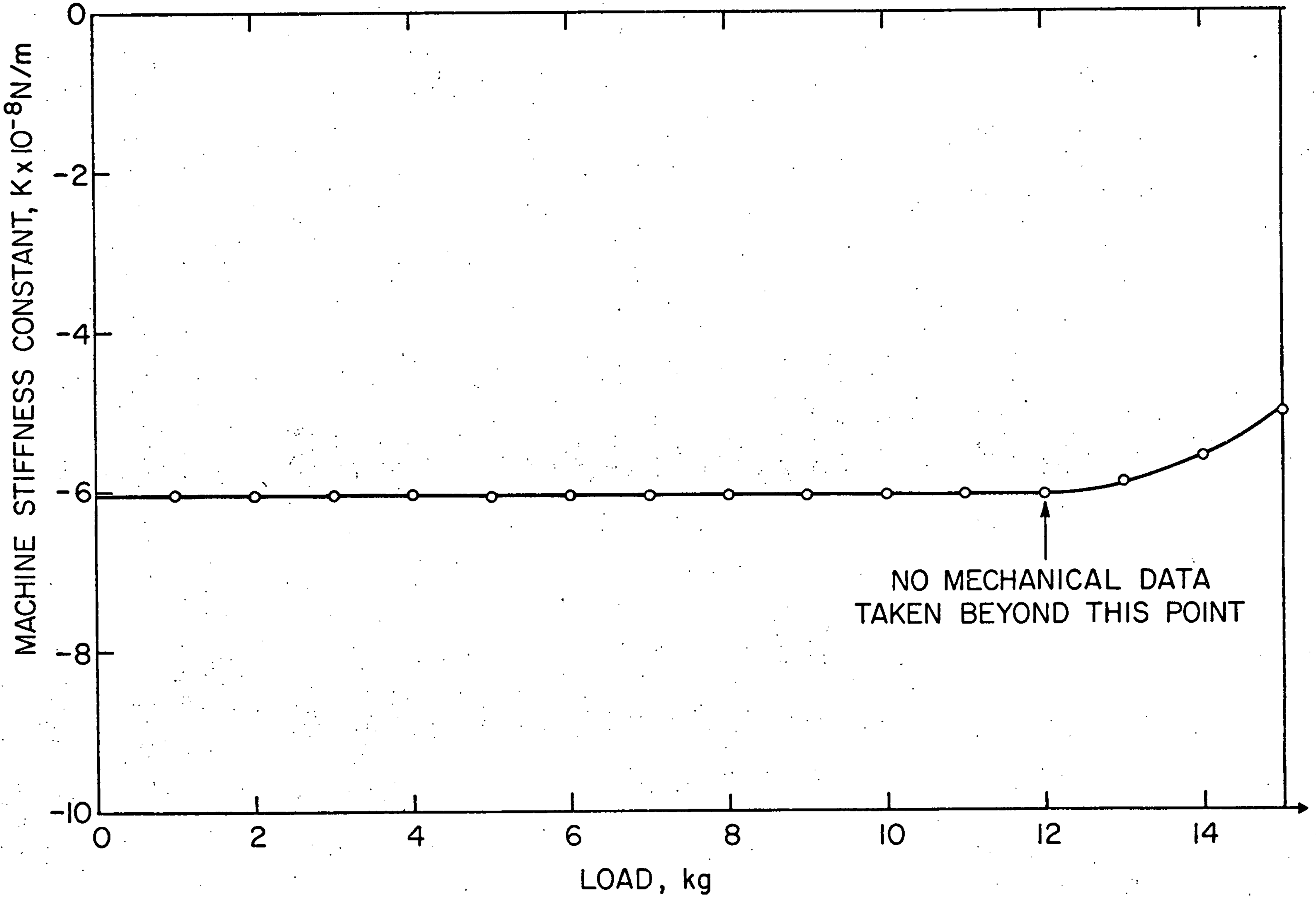
MACHINE STIFFNESS CONSTANT, K x 10^{-8} N/m
0
-2
-4
-6
-8
-10
0
2
4
6
8
10
12
14
LOAD, kg
NO MECHANICAL DATA TAKEN BEYOND THIS POINT

FIGURE 9

Figure 10

Relaxed moduli variations with stress amplitude for as-grown and outgassed samples. Note saturation occurs at approximately the same level for both samples.

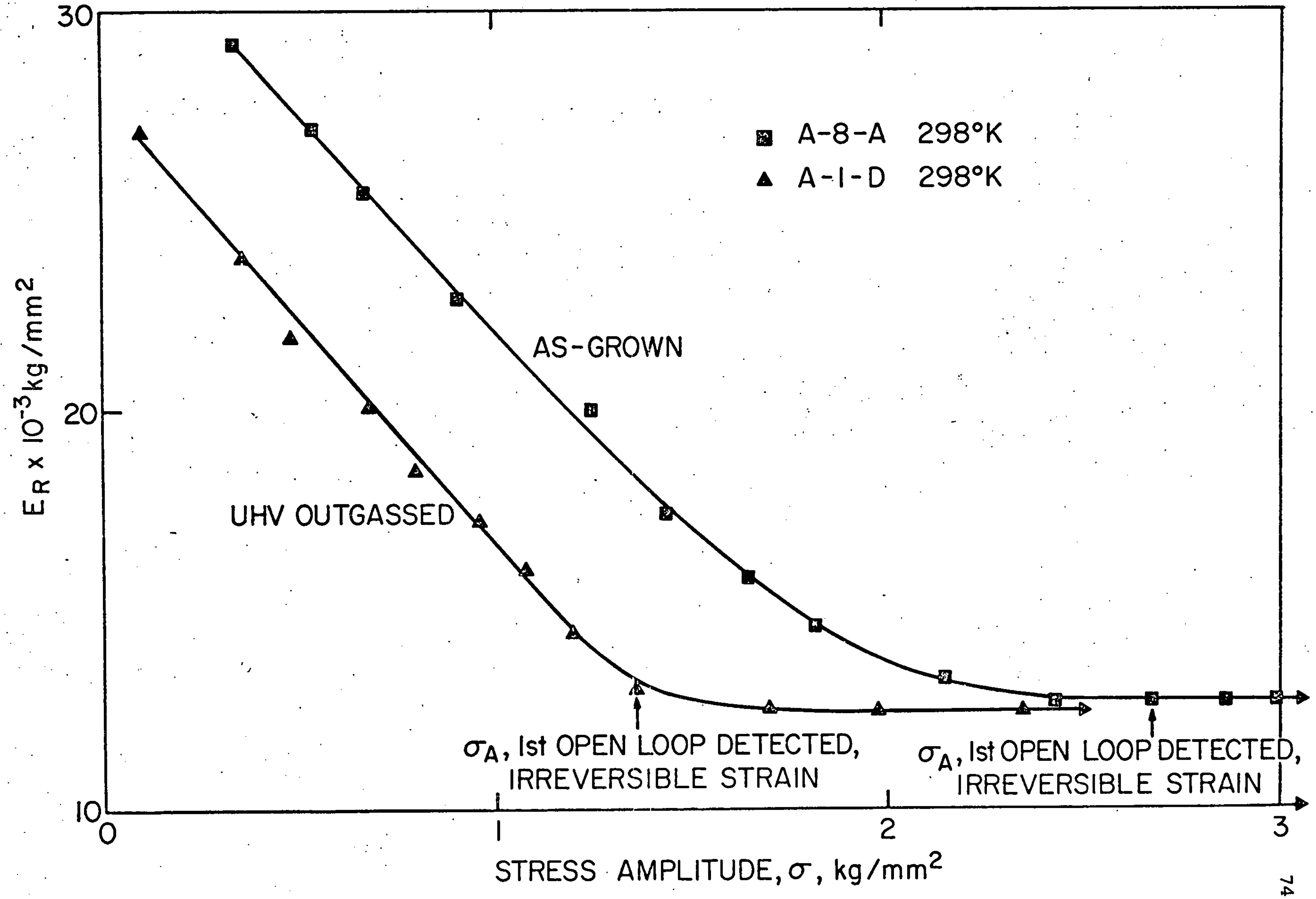
30
20
10
$E_R \times 10^{-3}$ kg/mm^2
0
1
2
3
STRESS AMPLITUDE, σ, kg/mm^2
▨ A-8-A 298°K
▲ A-1-D 298°K
AS-GROWN
UHV OUTGASSED
σ_A, 1st OPEN LOOP DETECTED, IRREVERSIBLE STRAIN
σ_A, 1st OPEN LOOP DETECTED, IRREVERSIBLE STRAIN

FIGURE 10

Figure 11

Modulus defect, $\Delta E/E_D$, as a function of stress amplitude, for three specimens of different purity levels: high oxygen and nitrogen content (A-8-A), high oxygen and low nitrogen level (B-2-D), and low oxygen and nitrogen impurity (A-1-D). Note defect saturates at approximately the same level in all three cases.

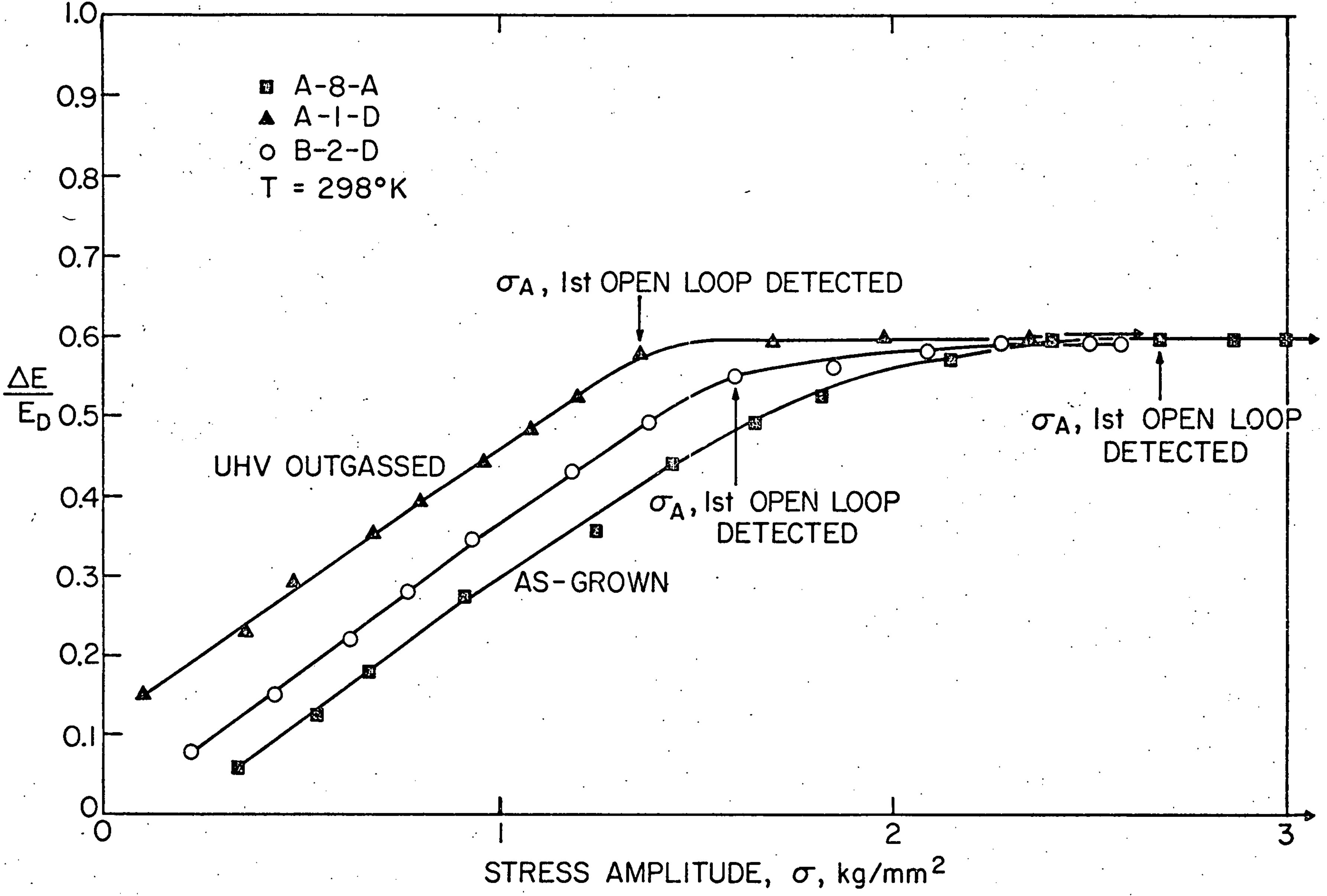
A-8-A
A-1-D
B-2-D
T = 298°K
σ_A, 1st OPEN LOOP DETECTED
σ_A, 1st OPEN LOOP DETECTED
σ_A, 1st OPEN LOOP DETECTED
UHV OUTGASSED
AS-GROWN
ΔE/E_D
STRESS AMPLITUDE, σ, kg/mm²
1.0
0.9
0.8
0.7
0.6
0.5
0.4
0.3
0.2
0.1
0
0
1
2
3

FIGURE 11

Figure 12

Typical load-unload traces. The initial slope, the relaxed modulus, E_R, shifts with increasing stress until saturation occurs when some plastic strain is observed for sensitivity $\sim 1\times10^{-6}$. Values of σ_E (stress amplitude at which the load-unload trace deviates from a straight line) and σ_A (stress amplitude at which the hysteresis loop opens irreversibly) are also shown.

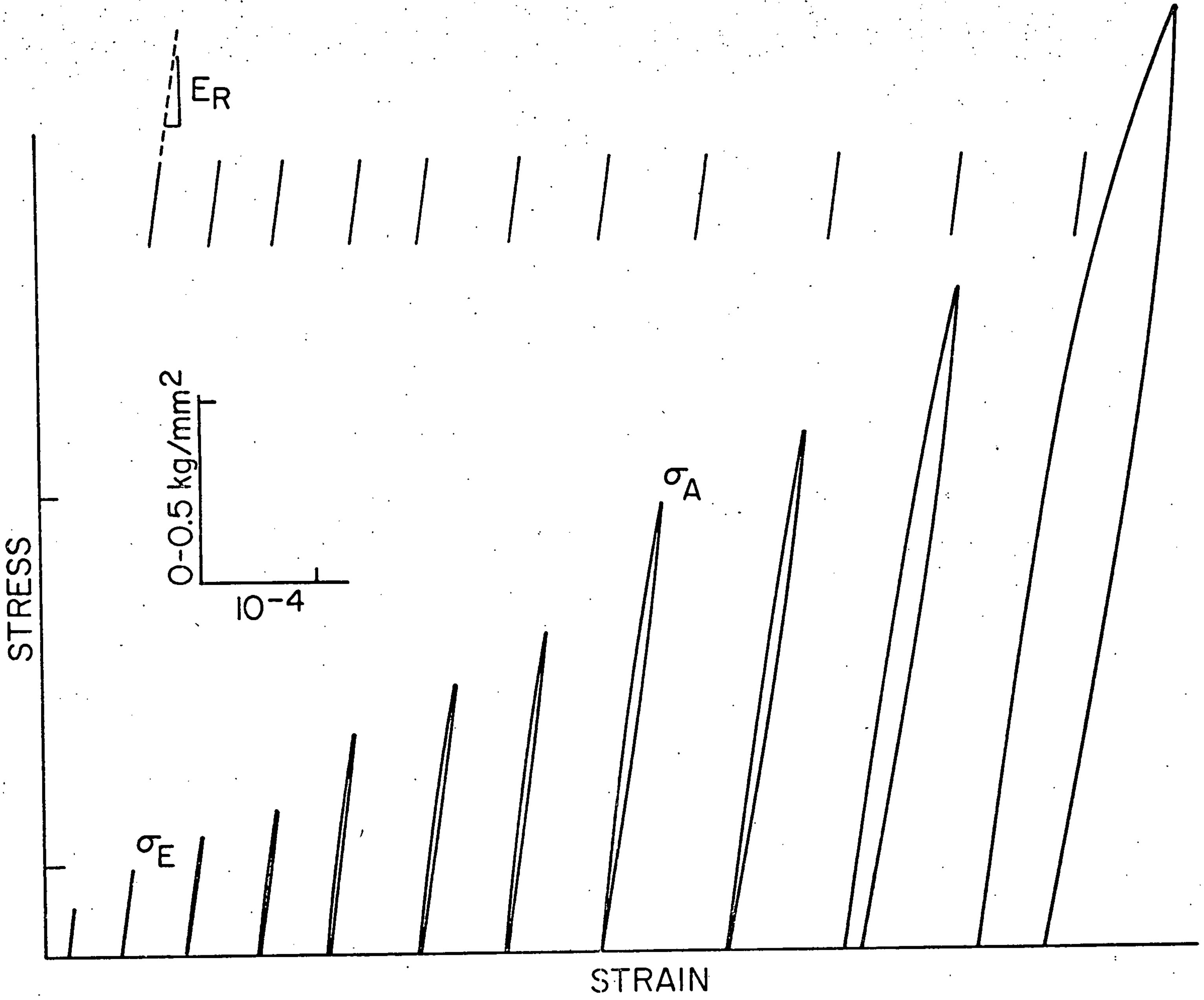

FIGURE 12

Figure 13

(a) Typical etch pit distribution of E surface of an unstrained as-grown sample.

(b) Change in etch pit distribution after a plastic strain $\sim 1\text{x}10^{-6}$ was observed. "New pits are circled and are observed to move in $\{110\}<111>$. The compression axis and the $\{110\}$ trace are indicated.

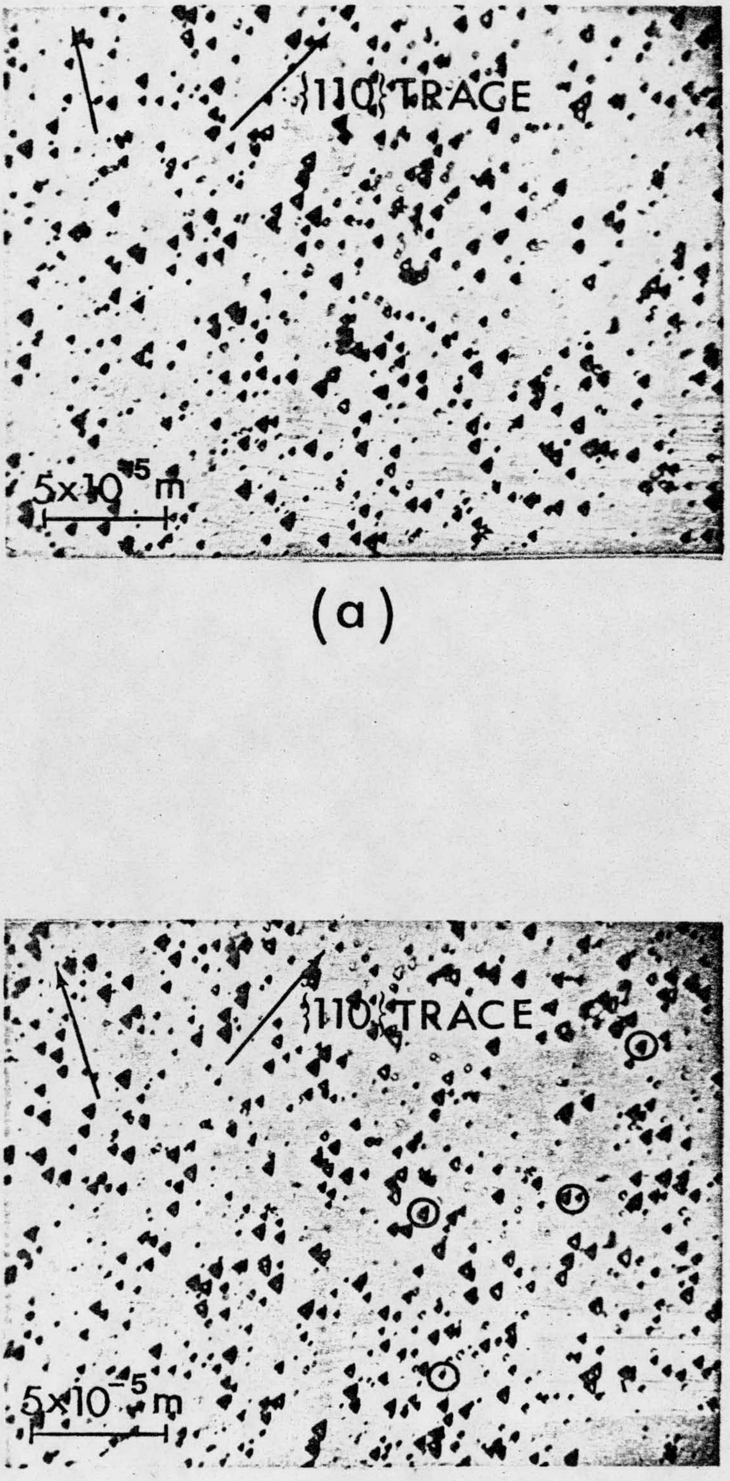

(a)

(b)

FIGURE 13

Figure 14

(a) Typical etch pit distribution of E surface of an unstrained outgassed specimen. Note the lower density compared to that of the as-grown case shown in Figure 13.

(b) Change in etch pit distribution after a plastic strain $\sim 1x10^{-6}$ was observed. "New pits are circled and are observed to move in $\{110\}<111>$. The compression axis and the $\{110\}$ trace are indicated.

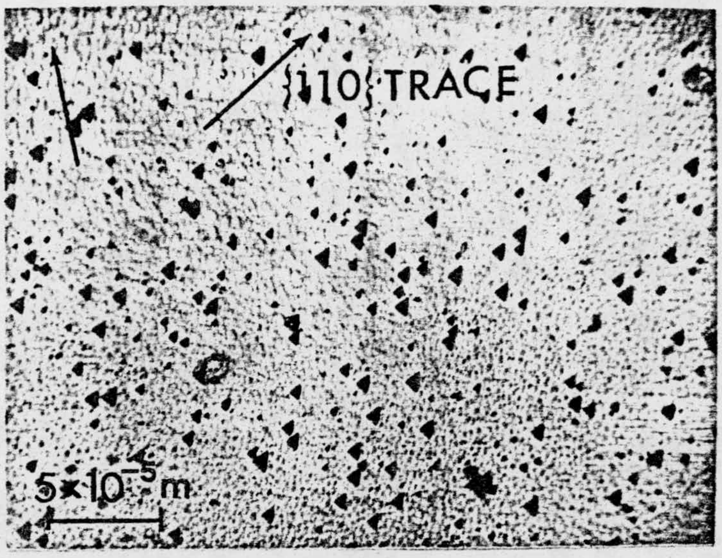

(a)

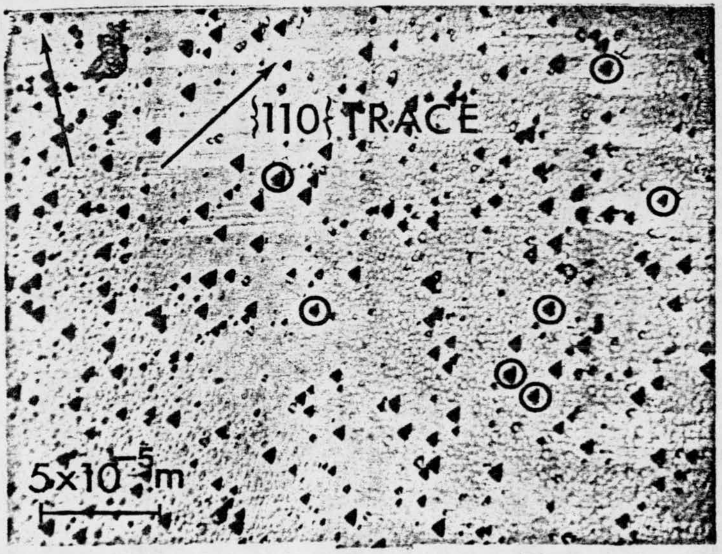

(b)

FIGURE 14

Figure 15

(a) Typical etch pit distribution of S surface of an unstrained as-grown specimen. Note the lower density of screw dislocations compared to edge dislocations as shown in Figure 13.

(b) Change in etch pit distribution after a plastic strain ~1x10^{-6} was observed. "New" pits are circled and are observed to move in $\{110\}<111>$. The compression axis and the $\{110\}$ trace are indicated.

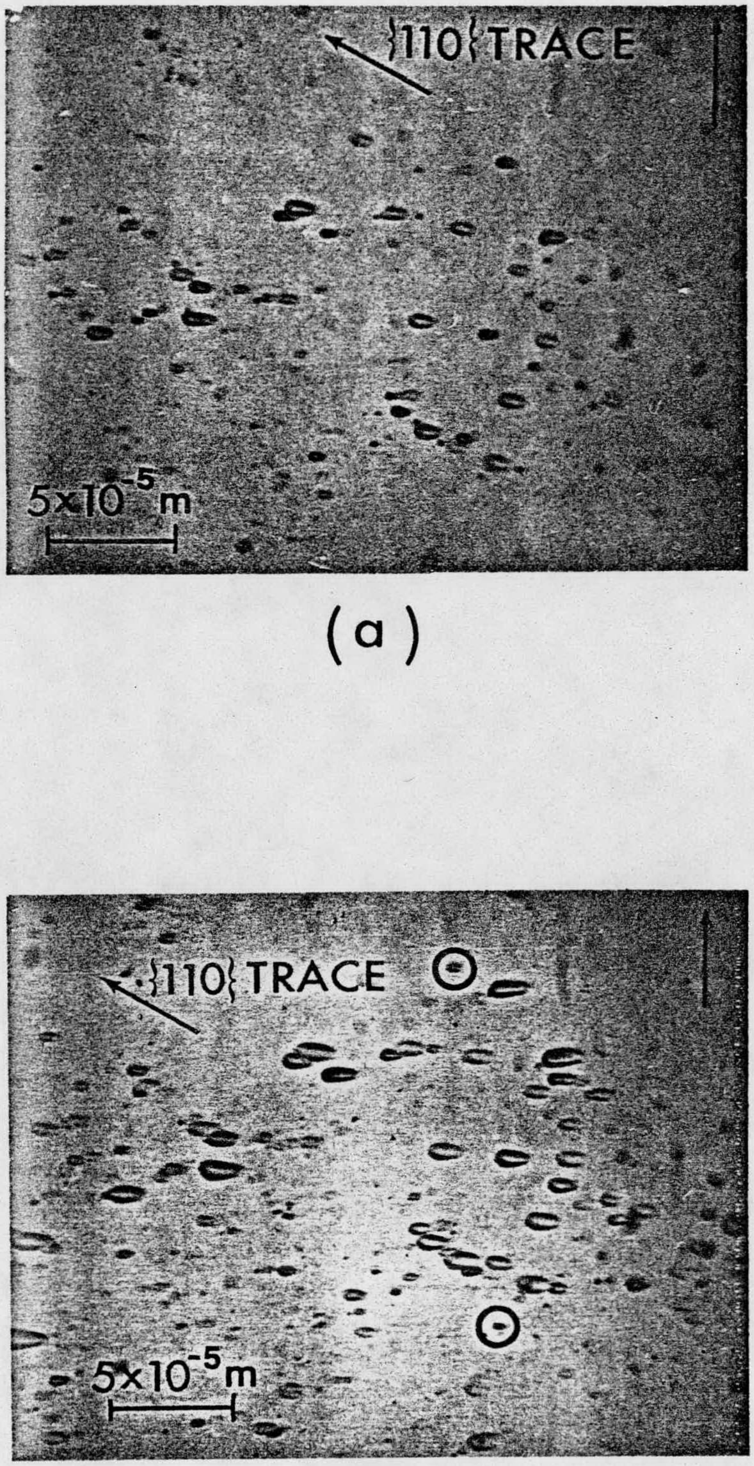

(a)

(b)

FIGURE 15

Figure 16

(a) Typical etch pit distribution of S surface of an unstrained outgassed specimen. Note the lower density compared to the as-grown case in Figure 14.

(b) Change in etch pit distribution after a plastic strain $\sim 1\times 10^{-6}$ was observed. "New" pits are circled and are observed to move in $\{110\}<111>$. The compression axis and the $\{110\}$ trace are indicated.

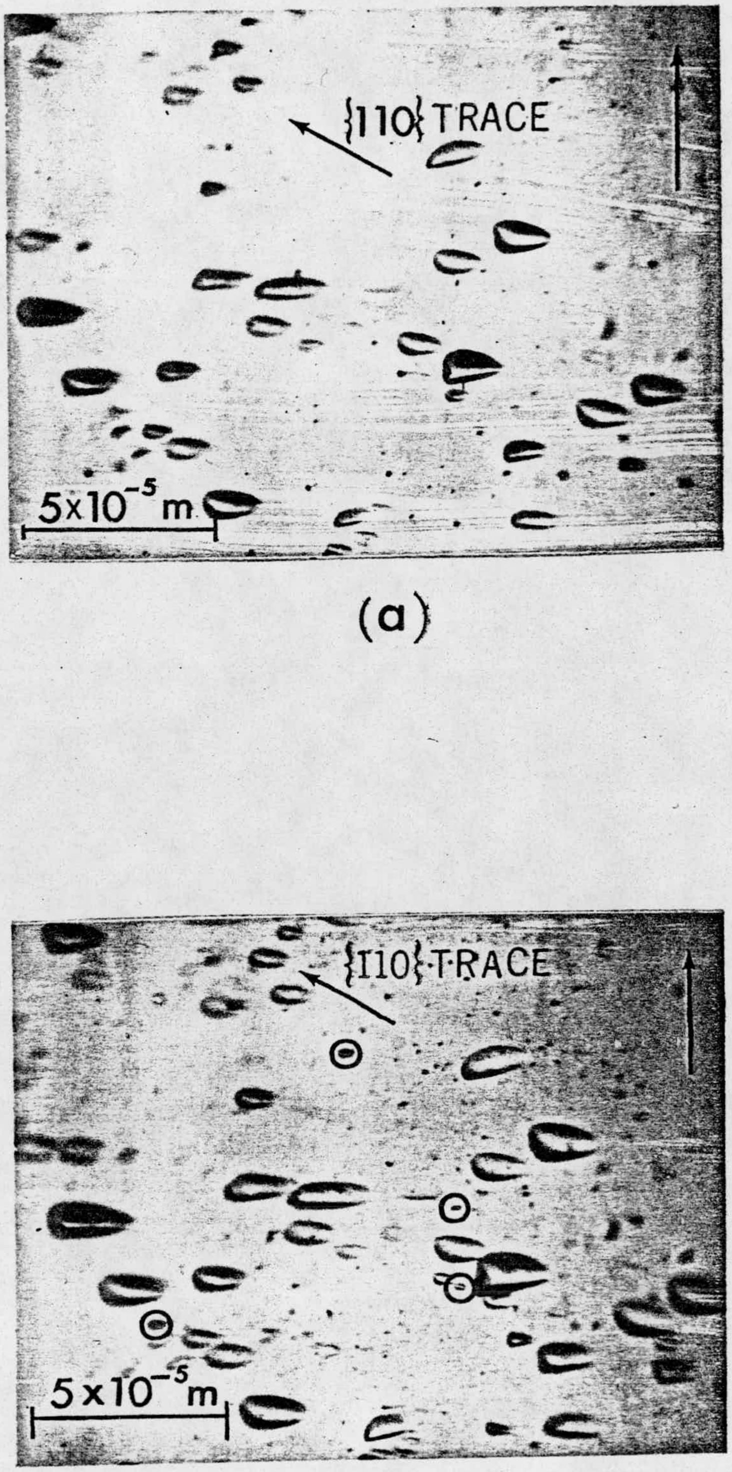

(a)

(b)

FIGURE 16

Figure 17

Variation of etch pit densities with plastic strain for outgassed and as-grown samples tested at 298°K and 77°K. Note the different densities observed on E and S surfaces and the higher percentage increase of pits for the outgassed samples.

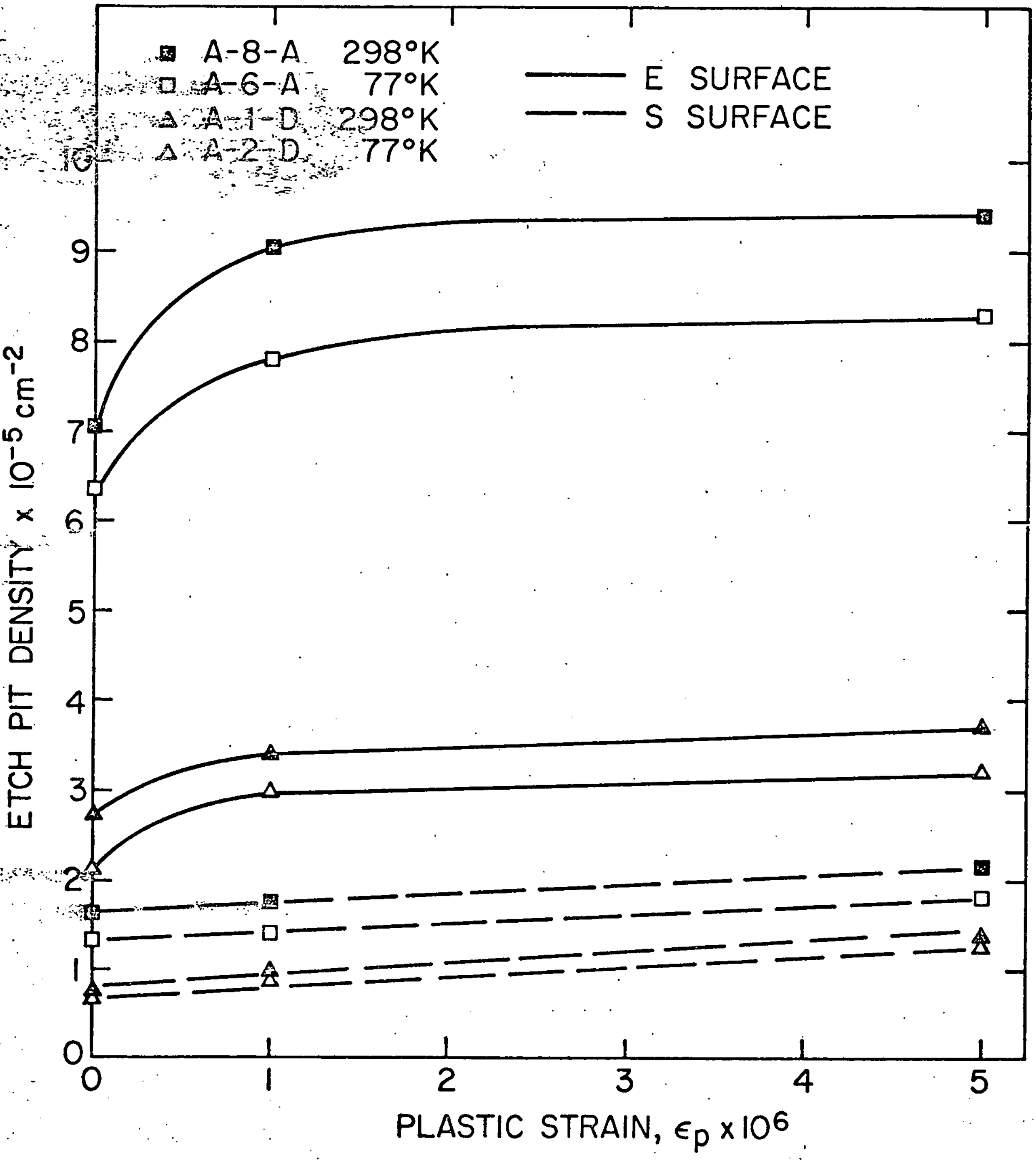
■ A-8-A 298°K
□ A-6-A 77°K
▲ A-1-D 298°K
△ A-2-D 77°K
E SURFACE
S SURFACE
ETCH PIT DENSITY x 10^{-5} cm^{-2}
0
1
2
3
4
5
6
7
8
9
10
PLASTIC STRAIN, ϵ_p x 10^6
0
1
2
3
4
5

FIGURE 17

Figure 18

Variation of etch pit densities with stress amplitude for outgassed and as-grown samples tested at 298^{o}K and 77^{o}K. Note different densities observed for E and S surfaces and outgassed and as-grown crystals.

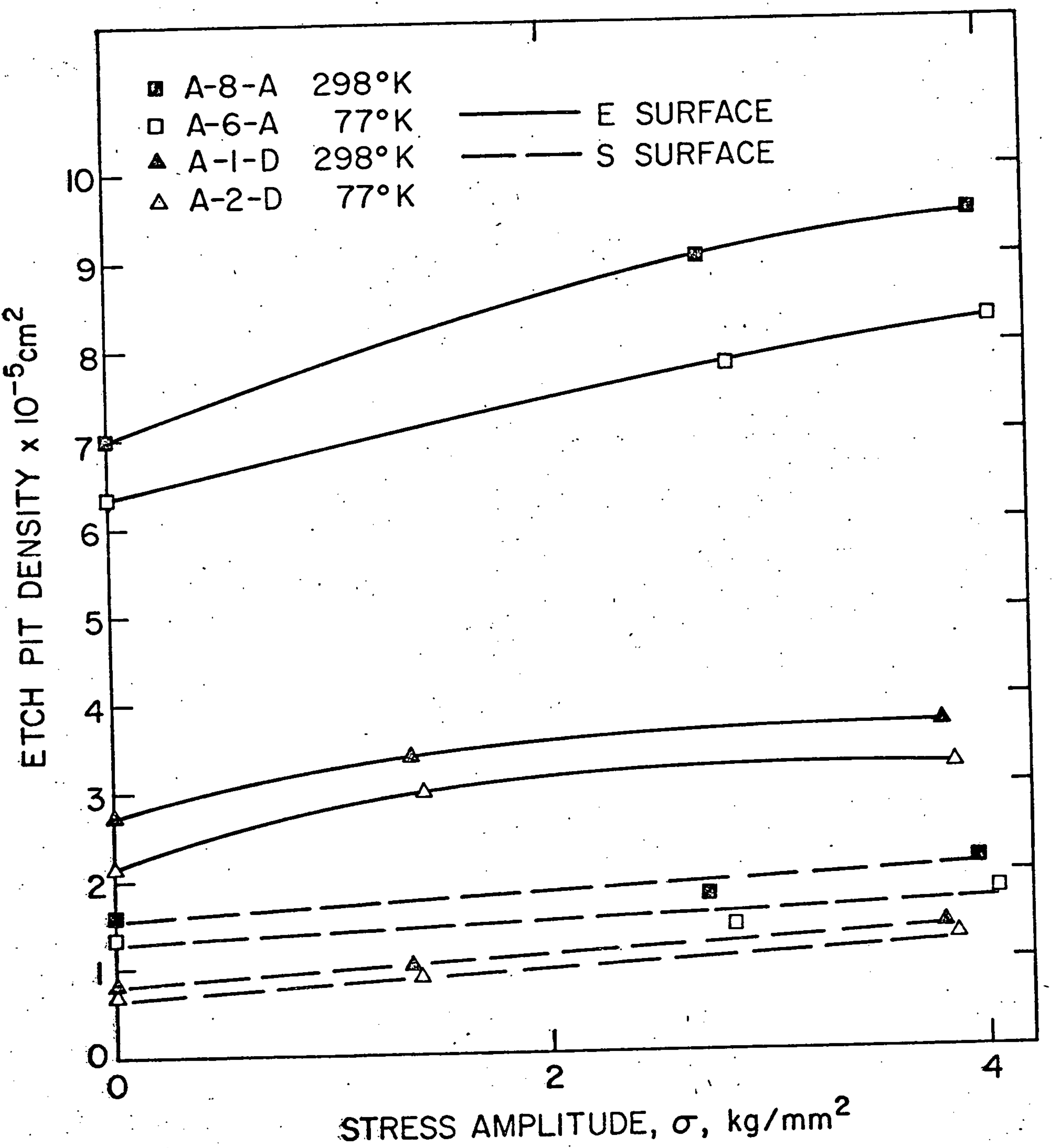
■ A-8-A 298°K
□ A-6-A 77°K
▲ A-1-D 298°K
△ A-2-D 77°K
E SURFACE
S SURFACE
ETCH PIT DENSITY x 10^{-5}cm^2
0
1
2
3
4
5
6
7
8
9
10
0
2
4
STRESS AMPLITUDE, σ, kg/mm^2

FIGURE 18

Figure 19

Dislocation velocities on E and S surfaces for outgassed and as-grown specimens as a function of permanent plastic strain for test temperatures $77^{o}K$ and $298^{o}K$. Velocities of edge and screw dislcations of outgassed specimens are faster than those of as-grown samples.

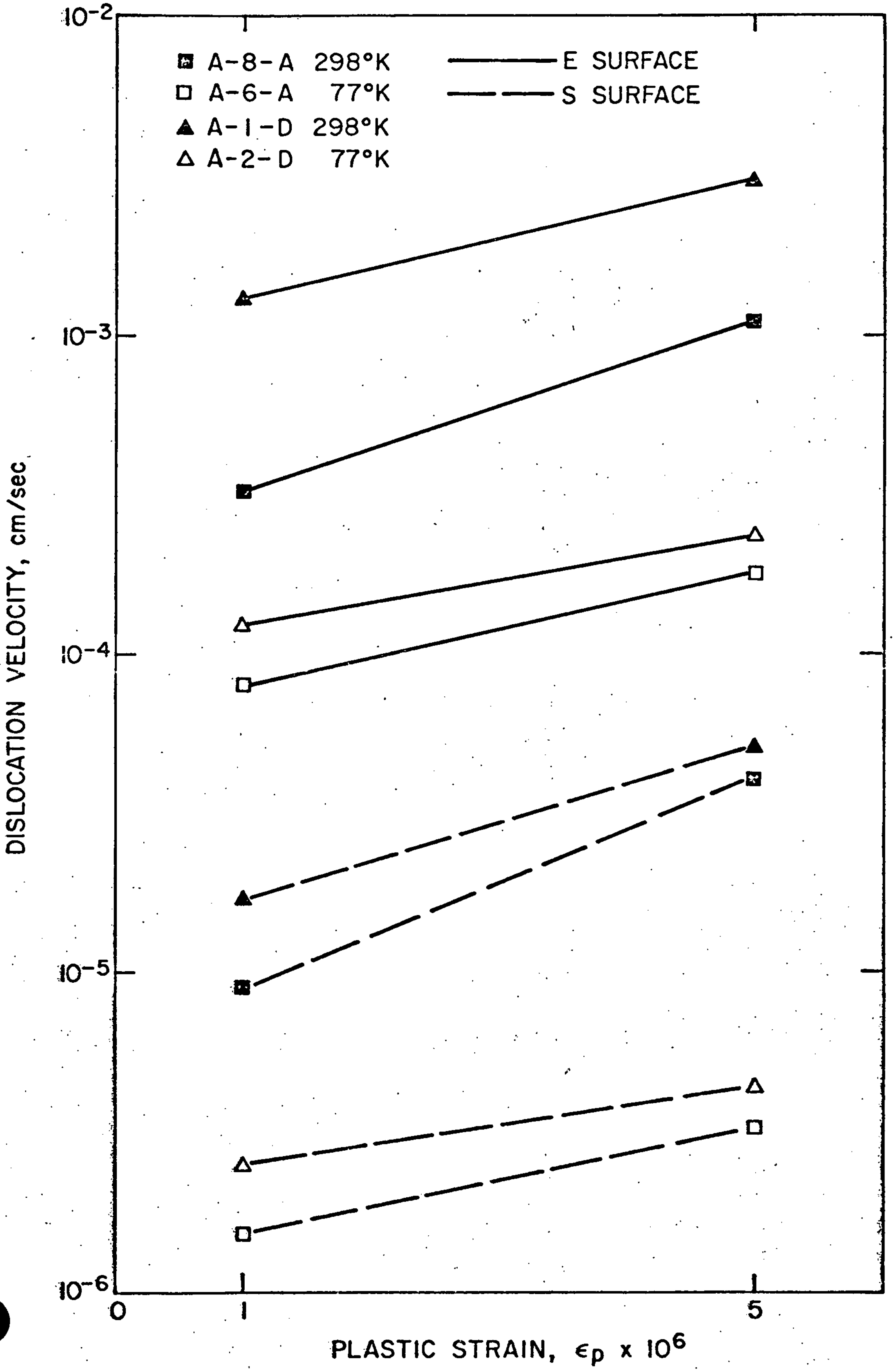
■ A-8-A 298°K
□ A-6-A 77°K
▲ A-1-D 298°K
△ A-2-D 77°K
E SURFACE
S SURFACE
DISLOCATION VELOCITY, cm/sec
10-2
10-3
10-4
10-5
10-6
0
1
5
PLASTIC STRAIN, εp x 10^6

FIGURE 19

Figure 20

Dislocation velocities on E and S surfaces for outgassed and as-grown specimens as a function of stress amplitude for test temperatures 77^{O}K and 298^{O}K. Velocities of edge and screw dislocations of as-grown specimens increase at a fast rate with stress amplitude.

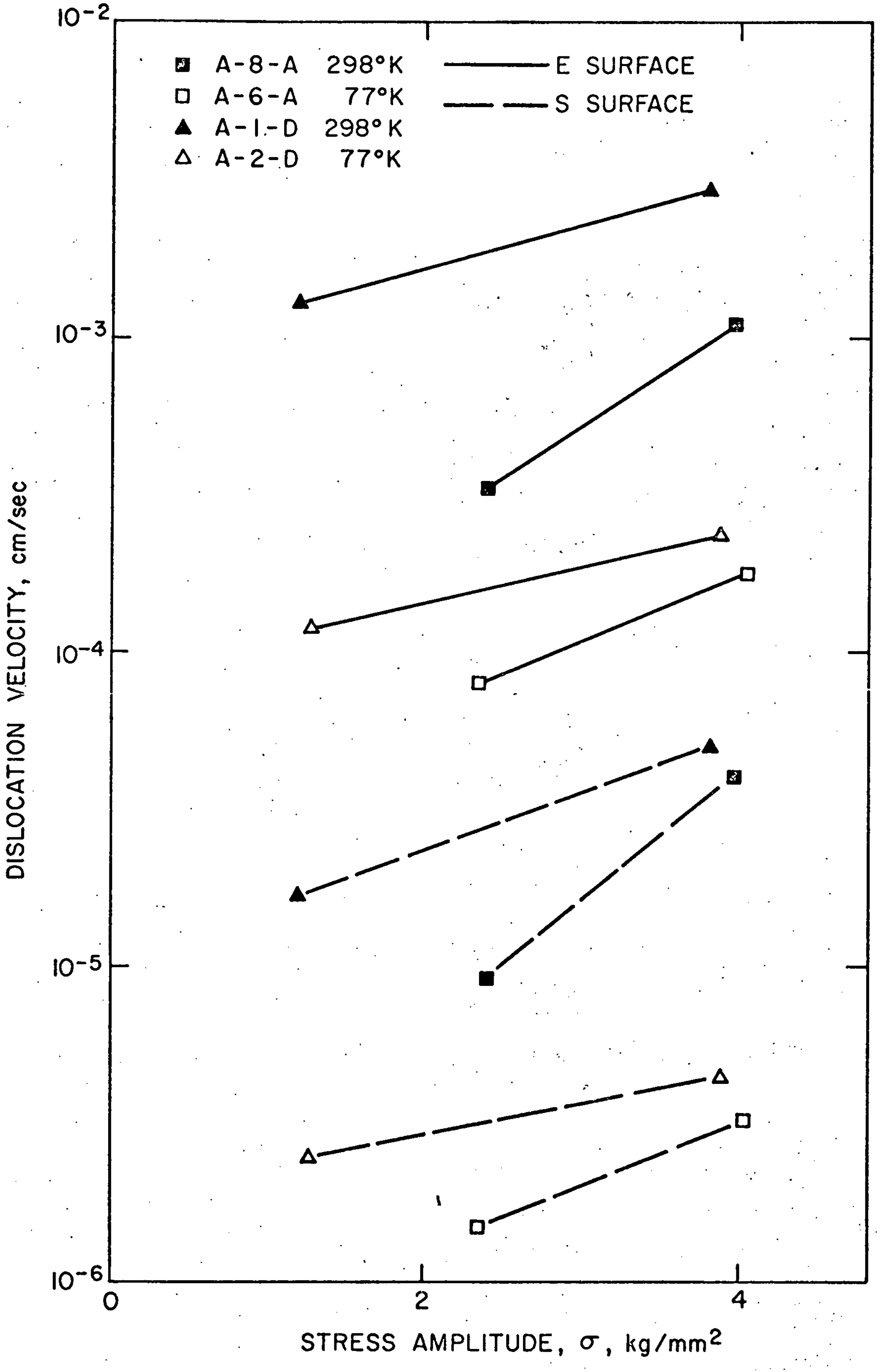
10^-2
10^-3
10^-4
10^-5
10^-6
0
2
4
DISLOCATION VELOCITY, cm/sec
STRESS AMPLITUDE, σ, kg/mm²
■ A-8-A 298°K
□ A-6-A 77°K
▲ A-1-D 298°K
△ A-2-D 77°K
E SURFACE
S SURFACE

FIGURE 20

ADDENDUM

It has been found that oxygen atoms, instead of molecules, are present in molybdenum as interstitial impurities. The calculations on page 53 should be:-

Avogadro's number, 16 g O = 6.02×10^{23} atoms

Number of O atoms per unit volume of Mo

$$= 6.02\times10^{23}\times10^{-3}/16 \text{ cm}^{-3}$$

$$= 3.76\times10^{19} \text{ cm}^{-3}$$

If O atoms are randomly distributed throughout crystal,

Distance between O atoms = $(3.76\times10^{19})^{-1/3}$ cm

$$l = 3.0\times10^{-7} \text{ cm}$$

Then, the binding energy $U_o = 0.4\times10^{-1}$ eV

If O atoms are totally on dislocation lines,

$$U_o = 0.25\times10^{-8} \text{ eV}$$